

1 Common mode signals and vertical velocities in the great Alpine area

2 from GNSS data

3 Francesco Pintori¹, Enrico Serpelloni^{1,2}, Adriano Gualandi¹

4 ¹Istituto Nazionale di Geofisica e Vulcanologia (INGV), Osservatorio Nazionale Terremoti, Roma, 00143, Italy.

5 ²Istituto Nazionale di Geofisica e Vulcanologia (INGV), Bologna, 40128, Italy.

6 *Correspondence to:* Francesco Pintori (francesco.pintori@ingv.it)

7 **Abstract.** We study the time series of vertical ground displacements from continuous GNSS stations located in the European
8 Alps. Our goal is to improve the accuracy and precision of vertical ground velocities and spatial gradients across an actively
9 deforming orogen, investigating the spatial and temporal features of the displacements caused by non-tectonic geophysical
10 processes. We apply a multivariate statistics-based blind source separation algorithm to both GNSS displacement time series
11 and to ground displacements modeled from atmospheric and hydrological loading, as obtained from global reanalysis models.
12 This allows us to show that the retrieved geodetic vertical deformation signals are influenced by environmental-related
13 processes and to identify their spatial patterns. Atmospheric loading is the most important one, reaching amplitudes larger than
14 2 cm. Besides atmospheric loading, seasonal displacements with amplitudes of about 1 cm are associated with temperature-
15 related processes and with hydrological loading, which both cause peculiar spatial features of GNSS ground displacements.
16 For example, temperature-related seasonal displacements show different behavior at sites in the plains and in the mountains.
17 Furthermore, while the displacements caused by atmospheric and hydrological loading are apparently spatially uniform, our
18 statistical analysis shows the presence of NS and EW displacement gradients.

19 We filter out signals associated with non-tectonic deformation from the GNSS time series to study their impact on both the
20 estimated noise and linear rates in the vertical direction. While the impact on rates appears rather limited, given also the long-
21 time span of the time-series considered in this work, the uncertainties estimated from filtered time-series assuming a power
22 law + white noise model are significantly reduced, with an important increase in white noise contributions to the total noise
23 budget. Finally, we present the filtered velocity field and show how vertical ground velocity spatial gradients are positively
24 correlated with topographic features of the Alps.

25
26 **Summary** We study time varying vertical deformation signals in the European Alps by analyzing GNSS position time series.
27 We associate the deformation signals to geophysical forcing processes, finding that atmospheric and hydrological loading are
28 by far the most important cause of seasonal displacements, together with temperature-related processes. Recognizing and
29 filtering out non-tectonic signals allows us to improve the accuracy and precision of the vertical velocities.

30 **1 Introduction**

31 The increasing availability of GNSS observations, both from geophysical and non-geophysical networks, pushed forward the
32 use of ground displacement measurements to study active geophysical processes on land, ice and on atmosphere, with
33 applications in a broad range of Earth science disciplines (e.g., Blewitt et al., 2018). Studies on active mountain building, in
34 particular, can now benefit from the use of GNSS vertical ground motion rates to get new insights into the contribution of the
35 different processes at work in the formation and evolution of mountain reliefs (e.g., Faccenna et al., 2014a; Sternai et al., 2019,
36 Dal Zilio et al. 2021, Ching et al. 2011). Proposed mechanisms of rock uplift rate include isostatic adjustment to deglaciation,
37 tectonic shortening, isostatic response to erosion and sediment redistribution, isostatic response to lithospheric structural
38 changes and dynamic adjustment due to sub-lithospheric mantle flow (e.g., Faccenna et al., 2014b). All these processes sum-
39 up to contribute to the actual vertical ground motion rates estimated from GNSS displacement time-series, and constraining
40 their relative contribution to mountain dynamics is challenging, because of the different spatial and temporal scales involved
41 and the short observational time period with respect to the characteristic timescales of the mentioned processes.

42 The availability of long-lasting (i.e., >8 yrs) GNSS position time-series minimizes the impact of transient and seasonal signals
43 in the vertical rate estimates (Masson et al., 2019). However, it is worth considering that GNSS measurements record ground
44 displacements due to a variety of multiscale processes (from continental-scale geodynamics and loading to local-scale
45 hydrology and tectonics), resulting in the presence of several deformation signals superimposed on the main linear trend, which
46 is commonly associated with geodynamic processes at the scale of current, decadal, geodetic observation window.

47 Excluding tectonic and volcanological processes, and once removed the effect of tides associated with solid earth, pole and
48 ocean, variations of atmospheric pressure loading and fluid redistribution in the Earth crust are the main cause of vertical
49 ground displacement recorded by GNSS stations worldwide (Liu et al. 2015). Atmospheric pressure and mass changes cause
50 time-variable displacement because of the elastic response of the Earth surface to these load variations, with vertical
51 displacements usually significantly larger than the horizontal ones, which appear as spatially-correlated signals with a
52 dominant one year period (e.g., Fu and Freymueller, 2012; Fu et al., 2012). Seasonal displacements are also caused by non-
53 tidal sea surface fluctuations. This process is of particular relevance in areas near the oceans, while in the inlands its effect is
54 significantly reduced (van Dam et al., 2012).

55 The presence of spatially-correlated signals in GNSS time-series can result from either the aforementioned large scale
56 processes, generally described as common mode signals (CMS), or processing errors, generally described as common mode
57 error (CME), like the mismodeling of displacements caused by solid Earth, ocean and atmospheric, and satellite orbits
58 mismodeling, which induces draconitic signals (Dong et al., 2006).

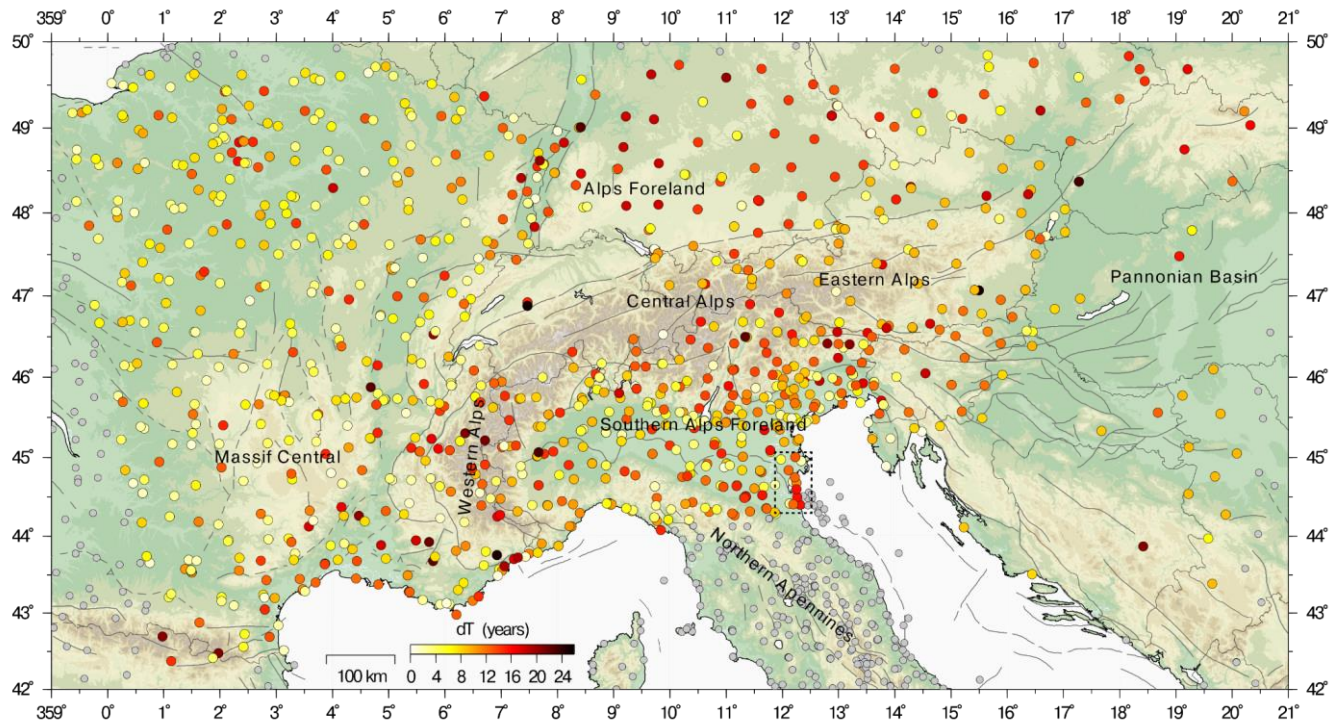
59 In the literature, the distinction between CMS and CME is not always clear, and spatially correlated signals are often removed
60 from the time series as CME without attempts of interpretation (e.g., He et al., 2017; Hou et al., 2019; Serpelloni et al., 2013;
61 Kreemer and Blewitt, 2021). Depending on the pursued goal, this approach can be fair. For example, if we were interested in
62 the study of long-term linear deformation, we might consider CMS as CME, but it is worth noting that the “CME” definition

63 for signals clearly associated with geophysical processes might be misleading. The removal of the CME/CMS in GNSS
64 position time-series, which is also known as time-series filtering, can help improve the precisions of the estimated linear
65 velocities. Moreover, a better understanding of CMS/CME origin can also provide new information on other deformation
66 mechanisms.

67 Here we use the European Alps as a natural laboratory to investigate the spatial and temporal contribution of different
68 geophysical processes, which we identify through a variational Bayesian Independent Component Analysis (vbICA), on the
69 vertical ground displacements recorded by a dense and spatially uniform network of continuous GNSS stations in the 2010-
70 2020 time-span. The Alps represent the highest and most extensive mountain range of Europe (see Fig. 1). We focus on the
71 vertical component, which is nominally less accurate and precise than the horizontal ones, because this mountain belt is
72 characterized by significant ground uplift and spatial vertical velocity gradients that are correlated with topography (Serpelloni
73 et al., 2013). The present-day convergence between Adria and the Eurasian plate is largely accommodated in the Eastern
74 Southern Alps (e.g., Serpelloni et al., 2016) where the Adriatic lithosphere underthrusts the Alpine mountain belt, and here
75 part of the observed vertical uplift is associated with active tectonics (Anderlini et al., 2020). Conversely, in other Alpine
76 domains, positive vertical velocities most likely derive from a complex interplay of deep-seated geodynamic and isostatic
77 processes (e.g., Sternai et al., 2019). In the Alpine framework, more accurate and precise measurements of geodetic vertical
78 ground motion rates can provide new constraints on the dynamics contributing to the ongoing vertical rates and their spatial
79 variations, with implications for the study of mountain building processes, response to deglaciation and active tectonics.

80 The structure of this work is as follows: in Section 2 we present methods commonly used for extracting spatially-correlated
81 signals in GNSS time series; in Section 3 we describe the data and methods used in this work; in Section 4 we characterize the
82 spatio-temporal behavior of three different independent datasets (GNSS vertical displacements, atmospheric and hydrological
83 loading models displacement time series) applying on each of them a vbICA decomposition and studying how they are related.
84 This allows us to spatially and temporally characterize the signals contributing to the measured GNSS displacement time series
85 and associate them with geophysical processes. We also estimate the vertical velocities and the noise features of the GNSS
86 stations after removing the non-tectonic signals identified with the vbICA analysis. In Section 5 we compare the results of
87 different filtering methods and use the results of our time-series analyses in order to evaluate the effects of the signal filtering
88 on the accuracies and precisions of the vertical velocities of the study region, which is of particular importance to better
89 characterize the processes generating the Alps uplift.

90



91

92 **Figure 1: Map of the study area showing the location of GNSS stations. Coloured circles show GNSS stations considered in the time-**
 93 **series analysis, with colours representing the length of the time-interval for which data are available at each station (0-25 years).**
 94 **The grey circles show GNSS stations not included in the time-series analysis to reduce contamination of deformation processes not**
 95 **associated with the Alps. Dark grey lines represent mapped faults from the Geodynamic Map of the Mediterranean. The dashed box**
 96 **includes GNSS stations affected by anthropogenic deformation signals (Palano et al., 2020).**

97 **2 Methods for the spatially-correlated signals extraction in GNSS time series**

98 Two widely used techniques for extracting CMS from a GNSS network are the Stacking Filtering Method (SFM, Wdowinski
 99 et al., 1997) and the Weighted Stacking Filtering Method (WSFM, Nikolaidis, 2002), which differs from the first because of
 100 a weighting factor based on the uncertainty associated with the GNSS data at each epoch.

101 Examples of time series filtering with the WSFM are provided by Ghasemi Khalkhali et al. (2021) in Northwest Iran, Jiang et
 102 al. (2018) in California and by Zhang et al. (2020) in China. The networks of the aforementioned studies span less than 1000
 103 km. However, when considering networks covering larger areas, the assumption that the CMS has uniform spatial distribution
 104 throughout the network is not valid (Dong et al., 2006; Tian and Shen, 2016; Ming et al., 2017), and the stacking methods
 105 become imprecise.

106 To take into account spatial heterogeneities, Tian and Shen (2016) propose an alternative stacking approach: the Correlation-
 107 Weighted Spatial Filtering (CWSF) method. Unlike the SFM, CWSF includes the spatial variability of CMS through a

108 weighting factor, which depends on the correlation coefficient between the residual position time series and on the distance
109 between the stations. Zhu et al. (2017) use CWSF to estimate the CMS on the Crustal Movement Observation Network of
110 China and discuss the effects of the thermal expansion and environmental loading, which includes atmospheric pressure
111 loading, non-tidal ocean loading and continental water storage. They find that while vertical CMS are mainly associated with
112 environmental loading, thermal expansion plays a minor role.

113 A filtering method similar to CWSF, called CMC Imaging, is developed and used by Kreemer and Blewitt (2021) in western
114 Europe to extract common mode components that are as local as possible. The main difference between CWSF and CMC
115 Imaging is that the former uses as a weighting factor both the distance and the correlation coefficient among the stations, while
116 the latter only the correlation coefficient, showing that it is representative of the distance among the stations. While the authors
117 do not explore the nature of the extracted CMS, they show that the CMC Imaging method is very effective in filtering out
118 CMS from GNSS time series, increasing the accuracy and precision of the velocity estimation. In particular, they show that
119 the minimum length of a time series needed to retrieve the long term velocity, within a given confidence limit, is almost halved
120 after the filtering.

121 Multivariate statistical techniques like Principal Component Analysis (PCA) and Independent Component Analysis (ICA) are
122 filtering techniques based on a completely different approach than stacking. Since they allow to take into account for the spatial
123 variability of CMS (Dong et al. 2006), ICA and PCA are used to characterize and interpret them. Multivariate statistics
124 techniques are also applied to study spatially-correlated seasonal displacements, which have been the target of several
125 researches in the last few years.

126 In California, Tiampo et al. (2004) associate a seasonal signal, extracted through the Karhunen-Loeve expansion technique,
127 with the combined effect of groundwater and pressure loading. In Taiwan, Kumar et al. (2020) find a close relationship between
128 atmospheric loading and CMS, extracted using a PCA; while Liu et al. (2017) apply a ICA to show that in the Nepal Himalaya
129 region annual vertical displacements are associated with atmospheric and hydrological loading.

130 Yuan et al. (2018) use three Principal Components (PCs) for CMS filtering over China, because of the presence of spatial
131 gradients related to the large extension of the study region. In that work, the authors show that environmental loading is one
132 of the sources of the CMS and that vertical GNSS velocities uncertainties are significantly reduced (54%) after CMS filtering.
133 Pan et al. (2019) find that the precision of the GNSS velocities, especially in the vertical component, increases after removing
134 spatially-correlated signals related to draconitic errors and to climate oscillation (La Niña - El Niño). The spatially-correlated
135 signals are identified by applying a PCA to the GNSS time series, where the linear trend and the seasonal signals are removed.
136 Pan's work is a good example of how vertical displacements are more affected by climate-related processes and data processing
137 errors than the horizontal ones, demonstrating that the vertical component is particularly worth analyzing with care.

138 The application of the ICA also proved effective for time series filtering, as shown by Hou et al. (2019): they identify spatially-
139 correlated signals and even though they do not provide an interpretation, classifying them as CME, they show that the precision
140 of the time series significantly increases after the filtering by ICA. Liu et al. (2015) use both PCA and FastICA algorithms

141 (Hyvärinen and Oja, 1997) to extract and interpret CMS as caused by atmospheric and soil moisture loading in the UK and the
142 Sichuan-Yunnan region in China.

143 Other examples of the influence of the non-tectonic processes on vertical velocity estimation are provided by Riddell et al.
144 (2020), who study the vertical velocities of the GNSS stations in Australia to estimate the contribution of the glacial isostatic
145 adjustment. One of the results of Riddell's work is the reduction of the vertical velocity uncertainty, achieved by first subtracting
146 the displacements associated with atmospheric, hydrological and non-tidal ocean loading from the GNSS time series, and then
147 filtering the residuals by applying both PCA and ICA.

148 The vbICA is a multivariate statistics-based blind source separation algorithm (Choudrey, 2002) implemented by Gualandi et
149 al. (2016) for solving the problem of blind source separation of deformation signals in GNSS position-times series and has
150 been successfully used to extract tectonic and hydrological transient deformation signals in (e.g., Gualandi et al., 2017a;
151 Gualandi et al., 2017b; Serpelloni et al., 2018). Larochelle et al. (2018) applied vbICA to study the relationship between GNSS
152 and Gravity Recovery and Climate Experiment (GRACE)-derived displacements in Nepal Himalaya and Arabian Peninsula,
153 with the goal of extracting seasonal signals and identifying the processes that generate them. Serpelloni et al. (2018) and Pintori
154 et al. (2021) use vbICA to characterize hydrological deformation signals associated with the hydrological cycle at a spatial
155 scale not resolvable by GRACE observations, separating ground water storage signals from other surface mass loading signals;
156 while Silverii et al. (2021) perform a vbICA decomposition on GNSS time series in the Long Valley Caldera region (California,
157 USA) to separate volcanic-related signals from other deformation processes, in particular the one associated with hydrology.
158 This method is also recently applied to InSAR data (Gualandi and Liu, 2021) to estimate the displacement caused by sediments'
159 compaction in San Joaquin Valley (California) and to separate a seasonal signal from the tectonic loading in the Central San
160 Andreas Fault zone.

161 **3 Data and Methods**

162 **3.1 GNSS dataset and time-series analysis**

163 Over the European plate, in particular, GNSS networks managed by national and regional agencies, provide a rather uniform
164 spatial coverage (e.g., <https://epnd.sgo-penc.hu/> and <https://gnss-epos.eu/>). Figure 1 shows the distribution of continuous
165 GNSS stations operating across the great Alpine area where, excluding Switzerland for which raw observations are not
166 accessible, GNSS stations cover, rather uniformly, both the mountain range and the European and Adriatic forelands. We
167 analyze the raw GPS observations using the GAMIT/GLOBK (Ver. 10.71) software (Herring et al, 2018), following the
168 standard procedures of the repro2 IGS reprocessing scheme (<http://acc.igs.org/reprocess2.html>). This is part of a large
169 processing effort, including >4000 stations in the Euro-Mediterranean and African region, where sub-networks, made by <50
170 stations, dynamically and optimally selected based on daily data availability, are processed independently with GAMIT and
171 later tied together using common, sub-net, tie sites and IGB14 core-stations, using the GLOBK software. The details of the
172 processing are given in the Supplementary Information S1. The result of our analysis is a set of ground displacement time-

173 series, realized in the IGB14 reference frame (<ftp://igs-rf.ign.fr/pub/IGb14>). The resulting position time-series (hereinafter
174 IGB14-time series) have been then analyzed in order to estimate, and correct, instrumental offsets due to changes in the station's
175 equipment setup, as extracted from sitelog or RINEX file headers.

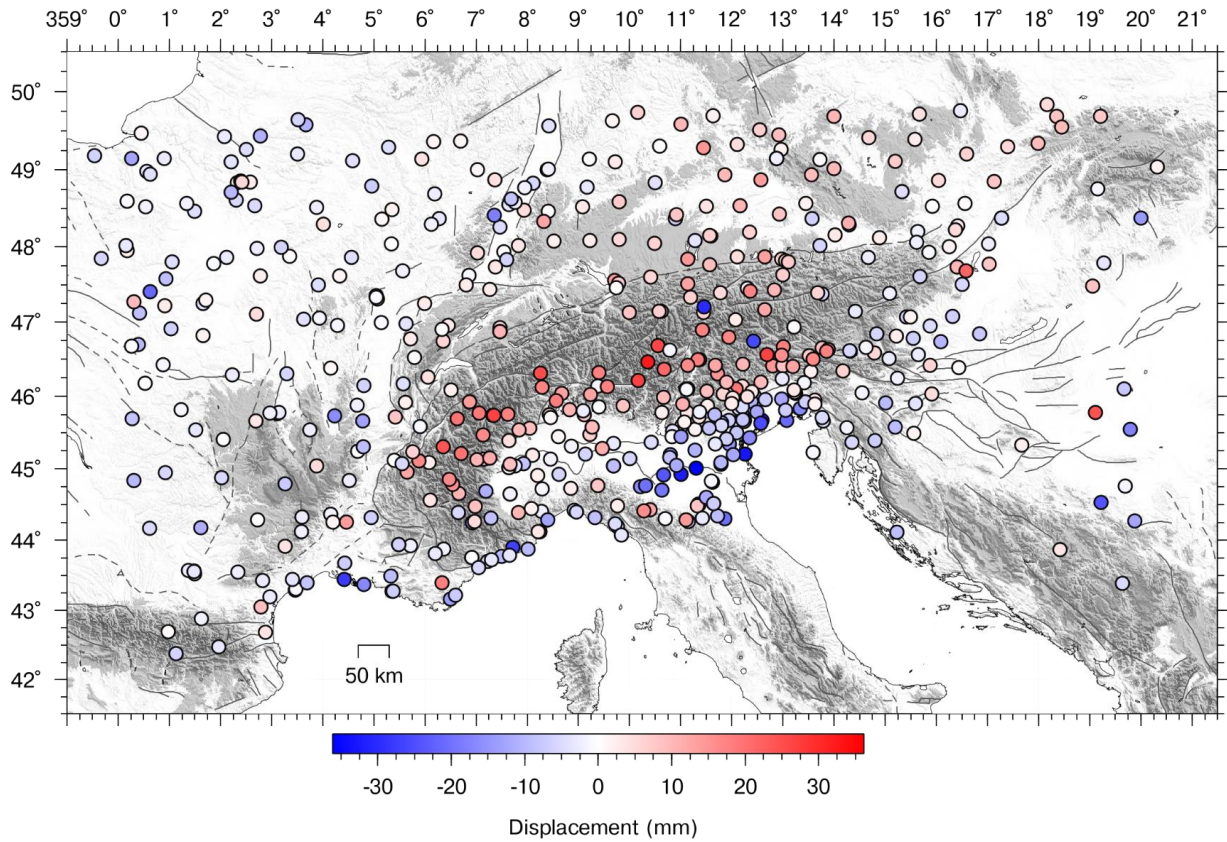
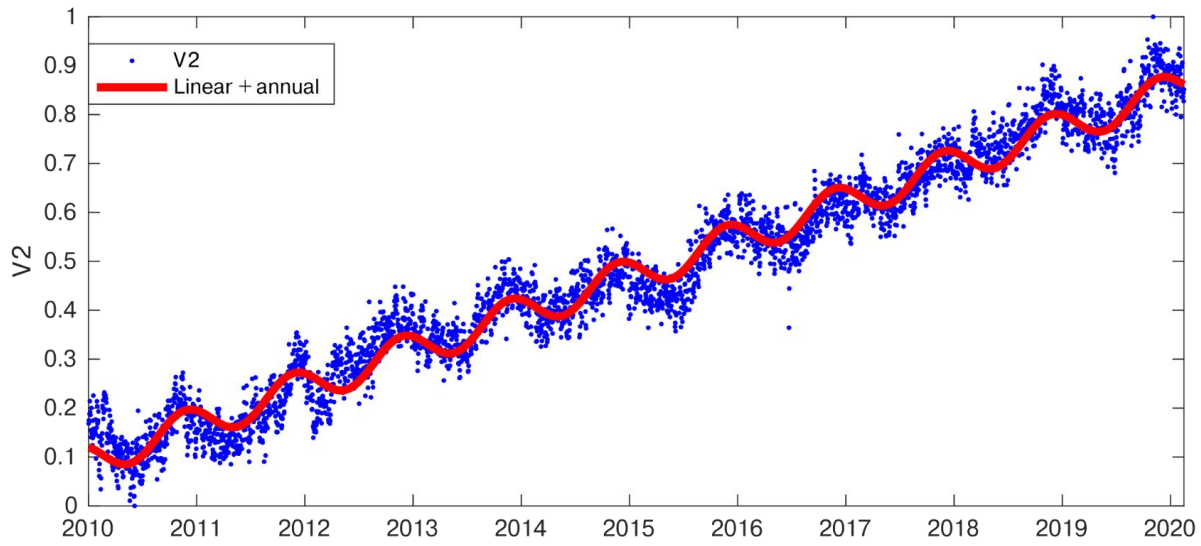
176 We consider the vertical displacement time-series of the stations between longitude 0° - 21° and latitude 42° - 50° N (see coloured
177 circles in Fig. 1) in the 2010-2020 time-span, excluding the sites in the northern Adriatic coast, known to be affected by
178 anthropogenic deformation signals (dashed box in Fig. 1) due to gas extraction (Palano et al., 2020) and the stations located in
179 the northern and central Apennines, where other tectonic and geodynamic processes are going on. We focus on the last decade,
180 in order to have the most uniform set of continuous measurements possible in, at least, a 10 years time-span. We acknowledge
181 that some of the stations shown in Fig. 1 have much longer time-series, but this time-interval maximizes the number of
182 simultaneous observations at many stations.

183 The IGB14 vertical displacement time-series are analyzed with the blind source separation algorithm based on vbICA
184 (Choudrey and Roberts, 2003; Gualandi et al., 2016). This technique falls under the umbrella of the so-called unsupervised
185 learning approaches, and it aims at finding statistically independent patterns that can be linearly combined to reconstruct the
186 original dataset. Differently from other commonly used ICA approaches, like for example FastICA (Hyvarinen and Oja, 1999),
187 the adopted vbICA is a modeling approach that uses a mix of Gaussians to reproduce the probability density functions (PDFs)
188 of the underlying sources. The variational Bayesian approach introduces an approximating PDF for the posterior parameters
189 of the model, and the cost function to be maximized is the Negative Free Energy of the model, which can be explicitly
190 calculated once a specific form for the approximating posterior PDF is chosen. This framework is particularly advantageous
191 because it allows for more flexibility in the description of the sources' PDF, giving the chance to model multimodal
192 distributions and to take into account missing data in the input time series.

193 The input time-series contains a secular motion, roughly representing the vertical rate in the IGB14 reference frame, which is
194 superimposed by a variety of signals, of different temporal and spatial signatures. The first step of our analysis is to estimate
195 a linear component to represent the secular motion and remove it from the time series. This is required by the fact that the
196 vbICA is more effective in separating the sources when the temporal correlation in the dataset is low. Here, rather than using
197 a classic trajectory model (e.g., Bevis and Brown, 2014) to model and detrend the original time-series, in order to avoid biases
198 in the estimates of station velocities due to the short length of the time series and to the possible presence of strong nonlinear
199 signals, we take this step in a multivariate sense as in Pintori et al. 2021. We perform a first ICA decomposition considering 8
200 components (or ICs). The number of components is determined by applying an F-test to establish if a more complicated model
201 is supported by the data at a 0.05 significance level (Kositsky and Avouac, 2010). The results of this analysis are reported in
202 Fig. S1, and show that one component, nominally IC2, contains a linear trend, with some cross-talk with a seasonal (annual)
203 signal, as shown in Fig. 2.

204 Before discussing the vbICA results, we briefly explain how to interpret the temporal evolution and the spatial distribution of
205 the ICs, so that it is possible to retrieve the displacements associated with them. The color of each GNSS site in Fig. 2 represents
206 the IC2 spatial response (U_2), which indicates the maximum displacement associated with the IC2, while the temporal function

207 V2 is normalized between 0 and 1. The displacement associated with IC2 between two epochs (e.g. t_1 and t_2 , with $t_2 > t_1$) at the
208 station n is computed as $V1(t_2) * U1_n - V1(t_1) * U1_n(t_1)$, where $V1(t_2)$ is the value associated with the temporal evolution of the IC
209 at the epoch t_2 . $U1_n$ depends on the site, but not on the epoch; its unit of measurement is mm, while V has no units of
210 measurement. As a result, $V1 * U1_n$ is in mm. It follows that if $U1_n$ is positive, as we observe for each station, and $V1$ is
211 increasing ($V1(t_2) > V1(t_1)$), the stations move upward during the $t_2 - t_1$ time interval. On the other hand, if $V1(t_2) < V1(t_1)$ the
212 stations move downward during $t_2 - t_1$. As regards Fig. 2, assuming $t_1 = 2010.0$ and $t_2 = 2020.0$, the displacements associated with
213 IC2 are ~ 30 mm upward at the “red” GNSS stations, ~ 30 mm downward at the “blue” GNSS stations and ~ 0 mm at the white
214 ones.



215

216

217

Figure 2: Temporal evolution and spatial response of the IC2 of the GNSS decomposition. Time series have been corrected only for instrumental offsets.

218

219 We fit a linear trend to the temporal evolution of IC2 (V2) using the function

220

$$221 \quad V2(t) = q + m \cdot t + A \cdot \sin(2\pi \cdot t + \varphi) \quad (1)$$

222

223 Once estimated m and q from (1) via a non-linear least square approach, we compute the displacements associated with IC2,
224 considering as its temporal evolution the function $y=q + m \cdot t$; then, we remove the computed displacements from each
225 original, IGB14, time series, obtaining the detrended dataset used in the subsequent decomposition step. The advantage of this
226 approach, compared to a trajectory model, is that it is not necessary to assume any temporal evolution of the deformation
227 signals a priori, except for the limited number of functions that make up Eq. (1). This is particularly advantageous in cases
228 where either transients of unknown origin or amplitude and/or phase fluctuations of the seasonalities are affecting some stations
229 and could lead to a mismodeling by a trajectory model. Notice in particular how signals potentially biasing the linear trend,
230 like the multi-annual ones in case of short time series, are separated from the IC representing the stations' velocities.

231 The results of the vbICA applied to the detrended time-series are shown and discussed in Sect. 4.1.

232 **3.2 Meteo-climatic datasets**

233 The results of the decomposition of the geodetic dataset are compared with the results obtained from the analysis of
234 displacement time-series associated with different meteo-climate forcings. In particular, here we consider hydrological,
235 atmospheric loading and precipitation from global, gridded, models. These time-series are analyzed with the vbICA method
236 already used for the geodetic dataset, and the results are compared in Sect. 3.2.

237 The Land Surface Discharge Model (LSDM), developed by Dill (2008), simulates global water storage variations of surface
238 water in rivers, lakes, wetlands, and soil moisture, as well as from water stored as snow and ice. The LSDM is forced with
239 precipitation, evaporation, and temperature from an atmospheric model developed by the European Centre for Medium-Range
240 Weather Forecasts (ECMWF). Using the Green's function approach, Dill and Dobslaw (2013) compute daily surface
241 displacements at 0.5° global grids caused by LSDM-based continental hydrology (hereinafter HYDL), and by non-tidal
242 atmospheric surface pressure variations (hereinafter NTAL). We also considered the *École et observatoire des sciences de la*
243 *terre* (EOST) loading service, which provides a model for the atmospheric and hydrological loading induced displacements.
244 Ground displacements are computed using the Load Love Numbers estimate from a spherical Earth model (Gegout et al.,
245 2010). The atmospheric loading is modeled using the data of the ECMWF surface pressure, assuming an Inverted Barometer
246 ocean response; the hydrological loading includes soil moisture and snow height estimated from the Global Land Data
247 Assimilation System (GLDAS/Noah; Rodell et al., 2004). All the datasets we have considered are provided in the center of
248 figure reference frame, have daily temporal resolution and spatial resolution of 0.5° . It is worth noting that neither LSDM-
249 based nor EOST models consider deep groundwater variations. GRACE data are often used to study hydrologically-induced
250 deformation associated with groundwater; in fact, through the analysis of the gravity field variations, it is possible to retrieve

251 changes through time of the water masses. GRACE has the advantage of being influenced by groundwater variations, which
252 are not taken into account by the HYDL model, but at the cost of a lower temporal (i.e., monthly) and spatial (~300 km)
253 resolution.

254 The precipitation data we use are provided by the NASA Goddard Earth Sciences Data and Information Services Center
255 (Huffman et al., 2019), they are daily with a spatial resolution of 0.1° .

256 **4 Results**

257 **4.1 Decomposition of GNSS time-series**

258 Figure 3 shows the result of the vbICA decomposition on the detrended displacement time-series, using 7 components as
259 suggested by the F-test.

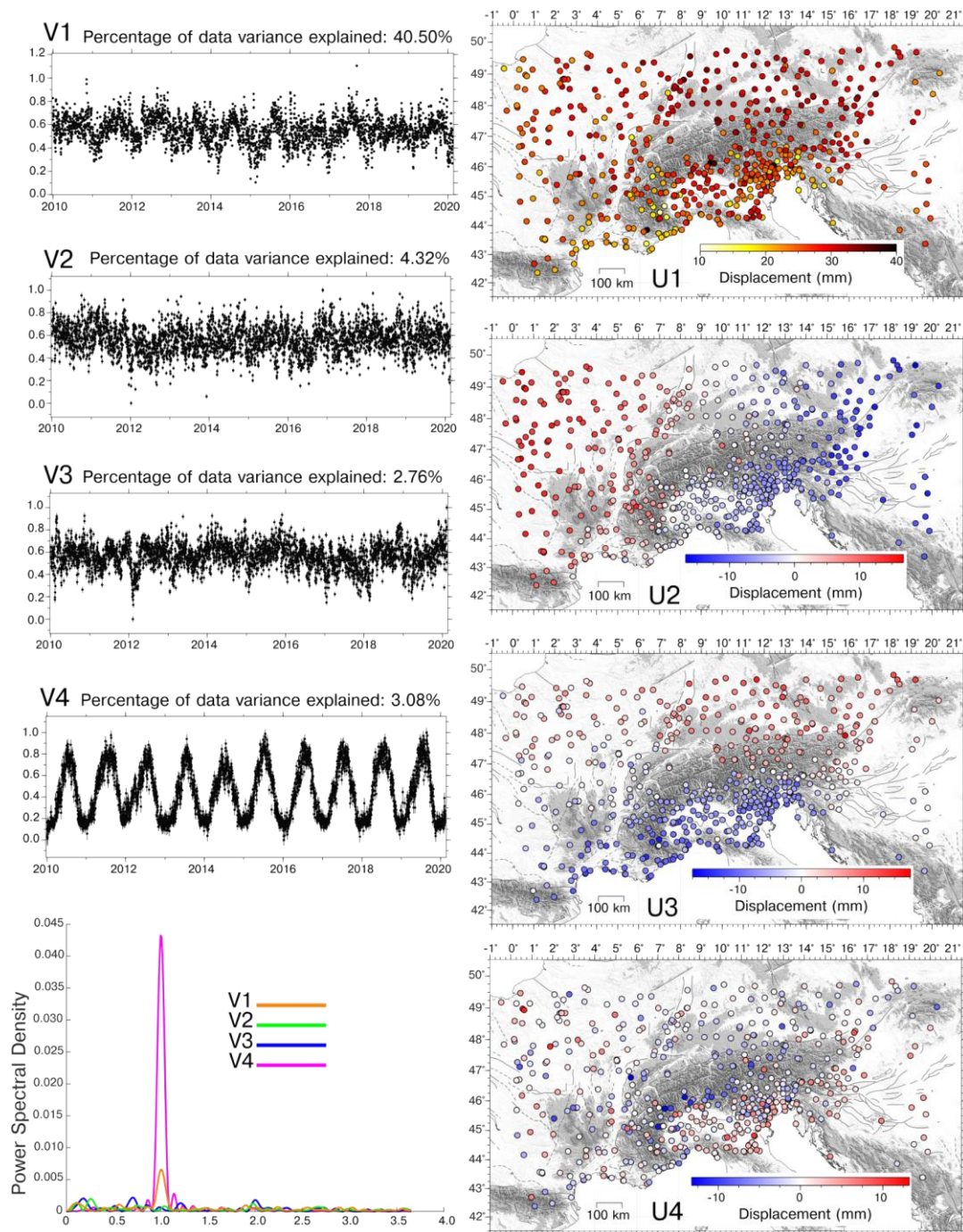
260 IC1 is a spatially uniform signal characterized by an annual temporal signature, as shown by the power spectral density (PSD)
261 plot in Fig. 3a.

262 The mean of the maximum amplitudes is 26 mm, while the histogram showing the distribution of displacement amplitudes is
263 shown in Fig. S4a.

264 IC2 shows a spatial response characterized by a clear E-W gradient, but, differently from IC1, its temporal evolution has not
265 a dominant frequency. The spatial response U2 of the eastern stations (in blue) is mainly negative, while the U2 of the western
266 stations (in red) is mainly positive. This means that when V2 is increasing the western (red) stations move up, while the eastern
267 (blue) ones move down. The sites in the central portion of the study area (in white) are very slightly affected by the IC2
268 component. The features of IC3 are analogous to those of the IC2, with the exception that a N-S gradient is present. The mean
269 of the amplitude of the absolute value of IC2 spatial distribution is 6.7 mm; and it is 5.6 mm for IC3. The histogram showing
270 the distribution of the absolute value is shown in Fig. S4b and S4c.

271 IC4 is an annual signal, as IC1, but with a heterogeneous spatial response: while some stations move upward some others
272 move downward. The mean of the amplitudes absolute value of the displacements is 2.7 mm; the relative histogram is shown
273 in Fig. S4d. The distribution of stations displaced with this phase difference seems to be mostly affected by geographical
274 features: the stations located in mountain regions subside when V3 increases, whereas the stations far from relief move upward.
275 The remaining three components are likely associated with local processes and discussed in the Supplementary Information
276 S3.

277



278
279
280

Figure 3: Temporal evolution, power spectral density and spatial response of: a) IC1; b) IC2; c) IC3; d) IC4.

281 4.2 GNSS vs environmental-related displacements

282 As discussed in the introduction, atmospheric and hydrological loading are likely the main sources of vertical displacement in
283 the great Alpine region. Since they are both uniform in terms of spatial response, showing smooth spatial variations, we decided
284 to check if the first 3 ICs of the GNSS decomposition are associated with the displacements due to atmospheric and
285 hydrological loading, and with their pattern of variability.

286 The vbICA analysis separates the data into statistically independent signals, which is useful because independent signals are
287 often caused by different and independent sources of deformation. Nonetheless, a single source of deformation, such as
288 atmospheric or hydrological loading, can be spatially heterogeneous and characterized by peculiar spatio-temporal patterns. In
289 this case, the vbICA separates a single source of deformation in different components associated with different spatio-temporal
290 patterns. As a consequence, we decided to apply a vbICA decomposition on HYDL and NTAL model displacement time series
291 in order to check if they show any pattern and if they resemble the spatial distribution of IC1, IC2 and IC3 of the GNSS
292 decomposition. NTAL and HYDL data have not been detrended.

293 We analyze with vbICA the hydrological loading (HYDL) and atmospheric pressure (NTAL) induced ground displacement
294 models (EOST and LSDM-based), in order to characterize the spatial pattern and temporal response associated with these
295 deformation sources, and study any possible link with the geodetic deformation signals described in Sect. 4.1. We use the
296 results of the global models to estimate the hydrological loading, even though we are aware that some local effects might not
297 be captured. In fact, considering the extension of the study area, it is very complicated to take into account the local features
298 needed to estimate the hydrological loading with a better precision than the one provided by the global models.

299 In particular, in this section we show the results obtained using the LSDM-based models because they take into account the
300 water stored in rivers, lakes and wetlands, while the EOST models do not. The results obtained using the EOST models are
301 presented in the Supplementary Information S2. Figure 4 and 5 show the spatial response, the temporal evolution and the PSD
302 of the ICs obtained using three components, to the NTAL (4) and HYDL (5) ground displacements. We decided to use three
303 components to reproduce the displacement patterns of IC1, IC2 and IC3 of the GNSS decomposition.

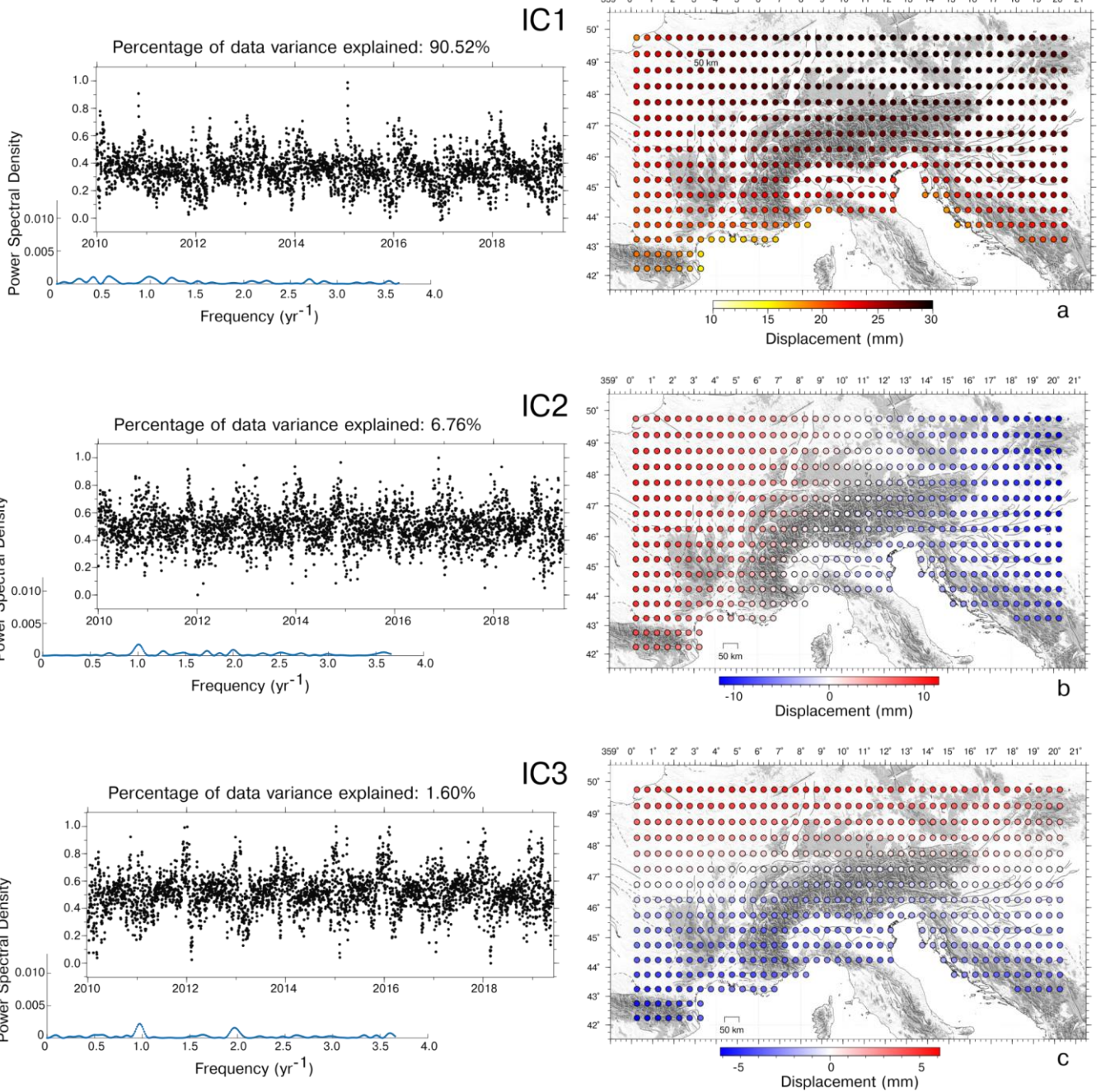
304 The first IC of both NTAL and HYDL shows a uniform spatial response, as IC1 of the GNSS dataset (Fig. 3a). The
305 mean/median amplitude of the maximum displacements associated with NTAL is very similar to GNSS both in terms of
306 mean/median amplitude (Table S1a) and distribution (Fig. 6, a); while for the HYDL model the amplitude is about two times
307 smaller than NTAL.

308 IC2 and IC3 of both NTAL and HYDL show E-W and N-S gradients in the spatial response, respectively, as observed for IC2
309 and IC3 of the GNSS dataset (Fig. 3b, d). Since the ICs spatial response of the NTAL and HYDL decomposition are very
310 similar, we also consider the sum of the displacement associated with NTAL and HYDL models, which can be considered as
311 “environmental loading”: we use the notation NTAL+HYDL_ICn to indicate the sum of the displacement associated with the
312 n-th component of the NTAL and HYDL decomposition. The amplitude of NTAL+HYDL_IC1, NTAL+HYDL_IC2 and

313 NTAL+HYDL_IC3 are only slightly lower than the ones of GNSS_IC1, GNSS_IC2 and GNSS_IC3, as shown in Fig. 6
314 (panels g,h,i) and in Table S1a.

315 Concerning the temporal evolutions, IC1 of the HYDL model is an annual signal, while the IC2 and IC3 PSD plots indicate
316 the presence of multi-annual signals. Unlike the HYDL decomposition, all the ICs of the NTAL decomposition contain the
317 annual frequency, in particular IC2, whereas IC3 also contains semiannual ones. It is also worth noting that the temporal
318 evolution of the ICs associated with the NTAL model are much more scattered than the ones resulting from HYDL, clearly
319 indicating that the displacements due to atmospheric pressure variations can show large fluctuations at daily timescale.

320 We also perform a vbICA decomposition on both datasets using two and four components, presented in the Supplementary
321 Information (Fig. S6 and S7). When using only two ICs, the results obtained (Fig. S6) are very similar to the first two ICs of
322 the 3-components decomposition. The first three ICs of the four component decompositions (Fig. S7) have both temporal
323 evolution and spatial distribution very similar to what is shown in Fig. 4 and Fig. 5. IC4 of the NTAL model has an annual
324 signature and a E-W gradient with a shorter wavelength compared to IC2, while IC4 of the HYDL decomposition has a NW-
325 SE gradient. This suggests that the N-S and E-W spatial patterns associated with the meteorological datasets are a robust feature,
326 being insensitive to the number of components chosen in the decomposition. It is also worth noting that the decompositions of
327 the NTAL and HYDL models explain the 98.89% and the 97.03% of the total variance when using 3 ICs, suggesting that
328 increasing the number of the ICs is not necessary. As a result, in the following discussion we refer to the results obtained from
329 the 3-components decomposition using the LSDM-based models, but remember that the results obtained using the EOST
330 models are fully comparable (Supplementary Information S2).



331

332

Figure 4: Temporal evolution, power spectral density and spatial response of IC1, IC2, IC3 of the NTAL model.

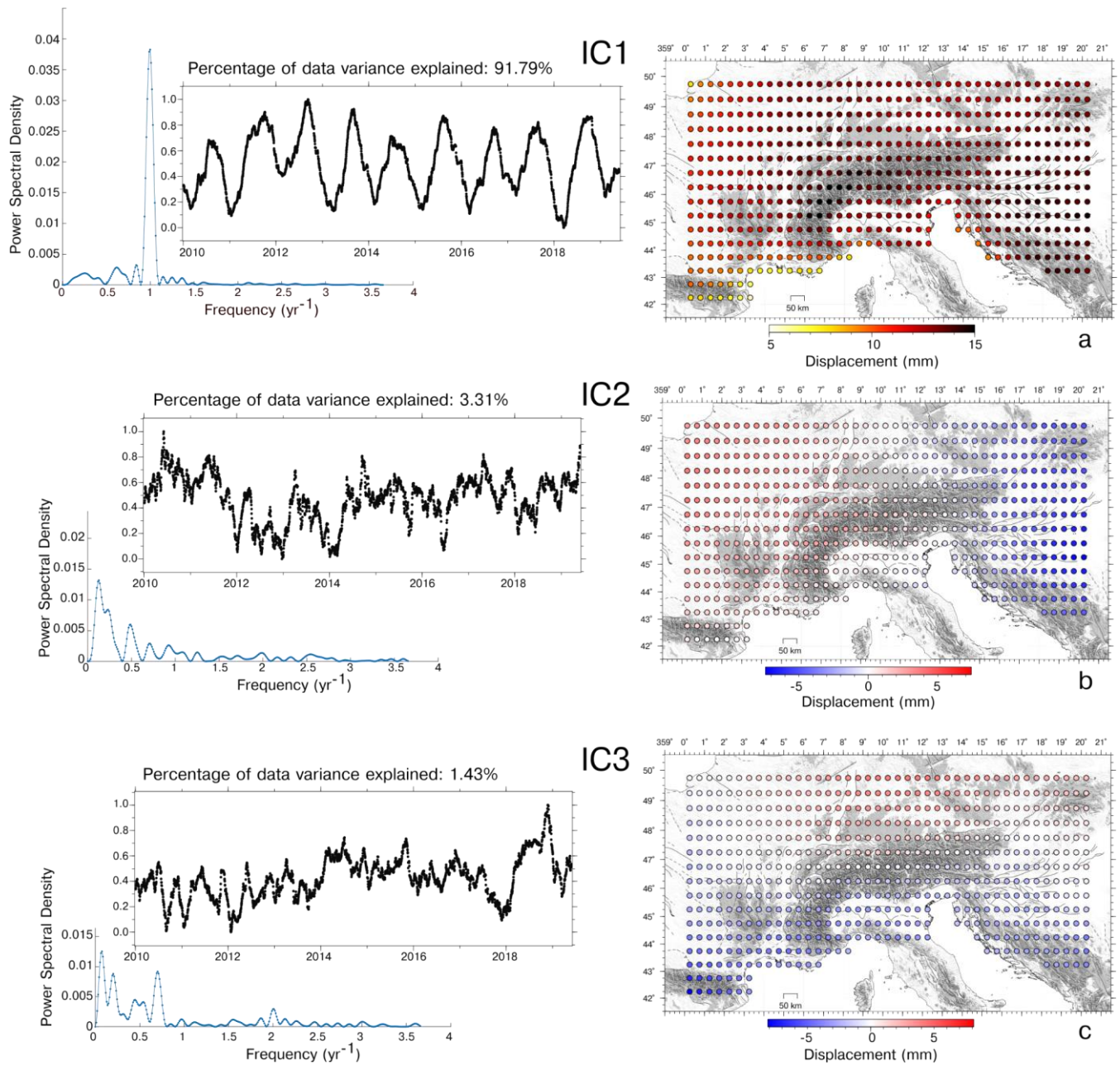
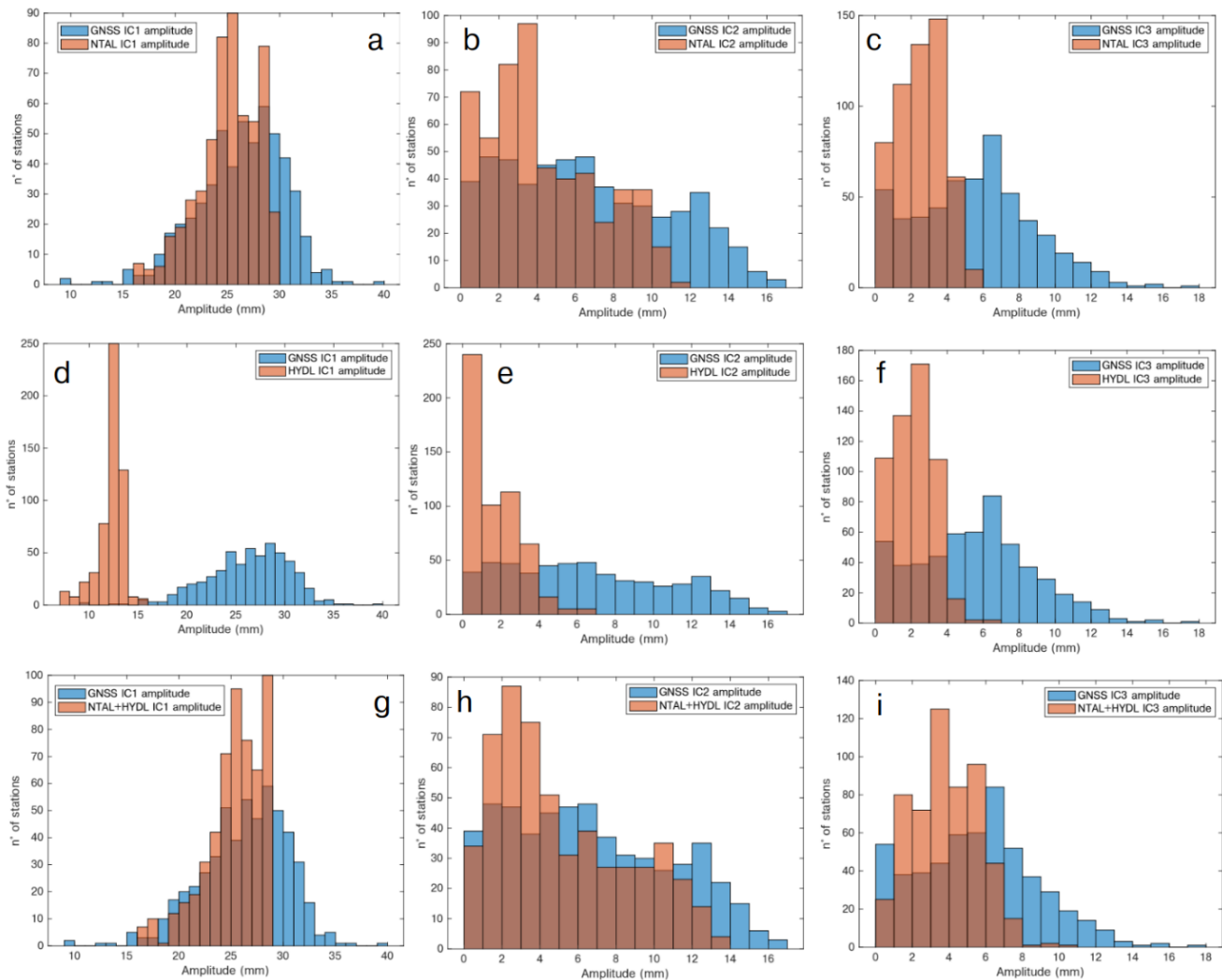


Figure 5: Temporal evolution, power spectral density and spatial response of IC1, IC2, IC3 of the HYDL model.

333
334
335



336

337

Figure 6. Histogram of the maximum displacements associated with:

338

(a) IC1 of the NTAL decomposition (orange), compared with the IC1 of the GNSS decomposition (blue); (b) same as (a) but

339

considering IC2; (c) same as (a) but considering IC3;

340

(d) IC1 of the HYDL decomposition (orange), compared with the IC1 of the GNSS decomposition (blue); (e) same as (d) but

341

considering IC2; (f) same as (d) but considering IC3;

342

(g) IC1 of the NTAL+HYDL decomposition (orange), compared with the IC1 of the GNSS decomposition (blue); (h) same as (g) but

343

considering IC2; (i) same as (g) but considering IC3.

344

345 In order to quantify the agreement between the displacements associated with the hydrological and atmospheric pressure

346

loading and the ICs of the GNSS dataset displaying consistent spatial patterns (IC1, IC2, IC3), we compute, for each GNSS

347

station, the Lin concordance correlation coefficient (Lin, 1989) between the displacement reconstructed by the ICs associated

348 with the different LSDM-based models. Unlike Pearson's correlation coefficient, Lin's one takes into account similarities on
349 both amplitudes and shapes of two time series.

350 The IC1 of the GNSS decomposition (GNSS_IC1) is compared with the first component of both NTAL (NTAL_IC1) and
351 HYDL (HYDL_IC1) datasets by associating each GNSS site with the nearest grid-point where NTAL and HYDL
352 displacements are computed.

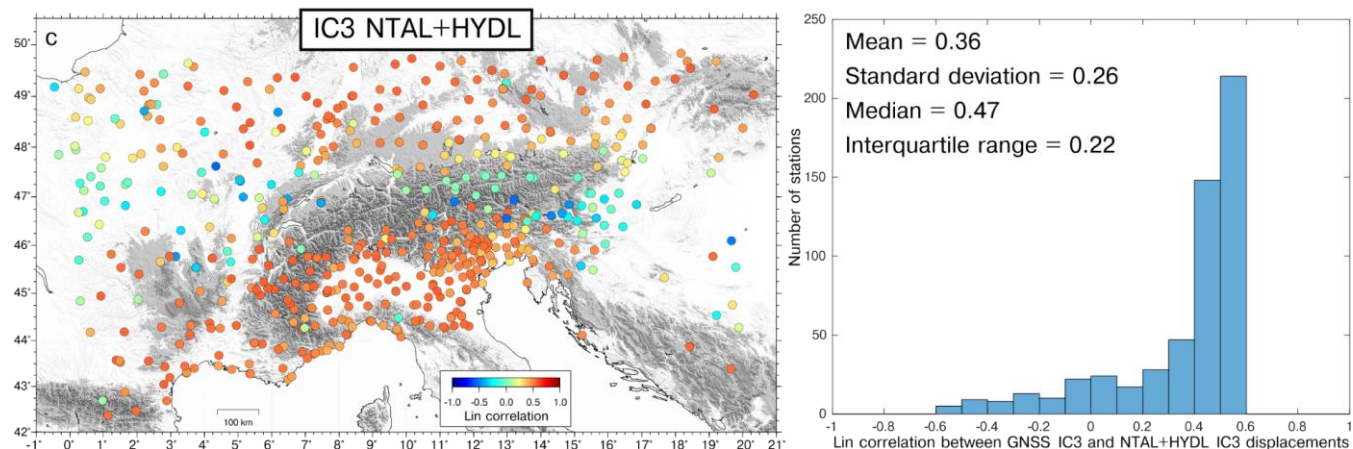
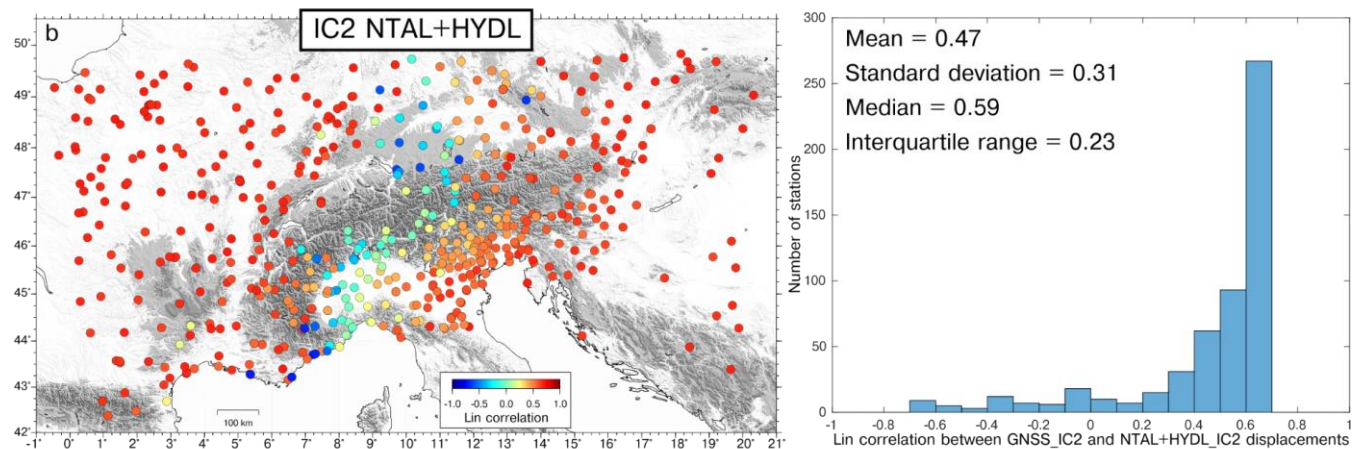
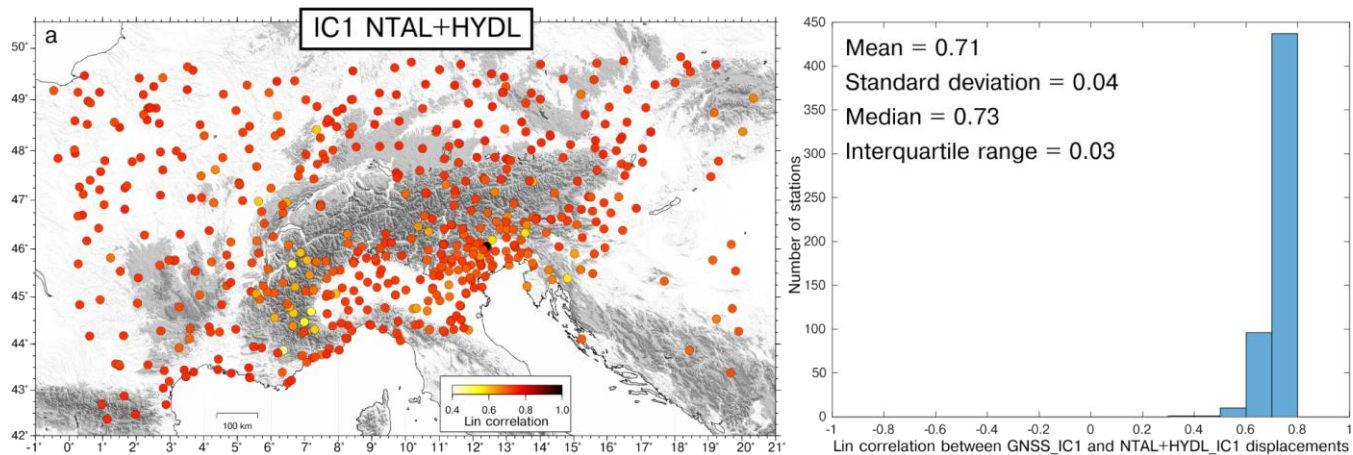
353 When considering the NTAL_IC1, we observe (Fig. S8a) a high temporal correlation with GNSS_IC1, while the correlation
354 between GNSS_IC1 and HYDL_IC1 is significantly lower (Fig. S9a). In both cases the value of the Lin correlation coefficient
355 is quite uniform in the dataset (~ 0.59 for NTAL_IC1 and ~ 0.35 for HYDL_IC1). The Pearson correlation is similar to Lin's
356 one (0.60 for NTAL_IC1 and 0.35 for HYDL_IC1), indicating that the amplitude of both NTAL_IC1 and HYDL_IC1 is
357 similar to the GNSS_IC1 amplitude. It is worth noting that if we consider NTAL+HYDL_IC1, the correlation with GNSS_IC1
358 increases to ~ 0.73 (Fig. 7a). As a result, we can interpret GNSS_IC1 as the combined contribution of NTAL and HYDL, where
359 NTAL plays the dominant role.

360 When considering IC2, we observe similar correlations between GNSS_IC2 and either NTAL_IC2 or HYDL_IC2 (Fig. S8b,
361 S8b). Nonetheless, in this case the correlation patterns are less uniform than the IC1 case, and few stations are even negatively
362 correlated with both NTAL_IC2 and HYDL_IC2 displacements. The sites where GNSS_IC2 displacements are negatively or
363 weakly correlated with NTAL_IC2 are the ones with the lowest IC2 amplitude. In fact, if we consider the stations whose
364 maximum displacements associated with GNSS_IC2 are larger than 3 mm, which are 411 out of 545, their mean Lin correlation
365 with NTAL_IC2 is 0.52; while the stations with amplitudes smaller than 3 mm have a mean correlation of 0.17. This is due to
366 the fact that, given the low displacements associated at these stations, the correlation is more sensitive to noise. The agreement
367 between the GNSS_IC2 and NTAL_IC2 is also confirmed by the Pearson correlation coefficient between the temporal
368 evolution of the two ICs, which is 0.63; while the Pearson correlation between GNSS_IC2 and HYDL_IC2 is 0.28. The same
369 pattern is observed when comparing GNSS_IC2 with NTAL+HYDL_IC2 (Fig. 7b): using 3 mm as threshold between large
370 and small GNSS_IC2 maximum displacements, the mean correlation is 0.57 for the stations most affected by this signal and
371 0.14 for the remaining ones. This suggests that also GNSS_IC2 is likely related to NTAL and HYDL loading processes.

372 The Lin correlation between GNSS_IC3 and NTAL+HYDL_IC3 resembles what just shown for IC2 (Fig. 7c): at sites where
373 the GNSS_IC3 maximum amplitude is larger than 3 mm, which are 414 out of 545, the mean correlation with
374 NTAL+HYDL_IC3 is 0.44; while it is 0.10 for the remaining ones. As for IC1, both GNSS_IC2 and IC3 displacements are
375 best reproduced when considering the combined effect of NTAL and HYDL (see Fig. S8c, S9c compared to Fig. 7). The
376 Pearson correlation between GNSS_IC3 and NTAL_IC3 is 0.47; while between GNSS_IC3 and HYDL_IC3 is 0.30.

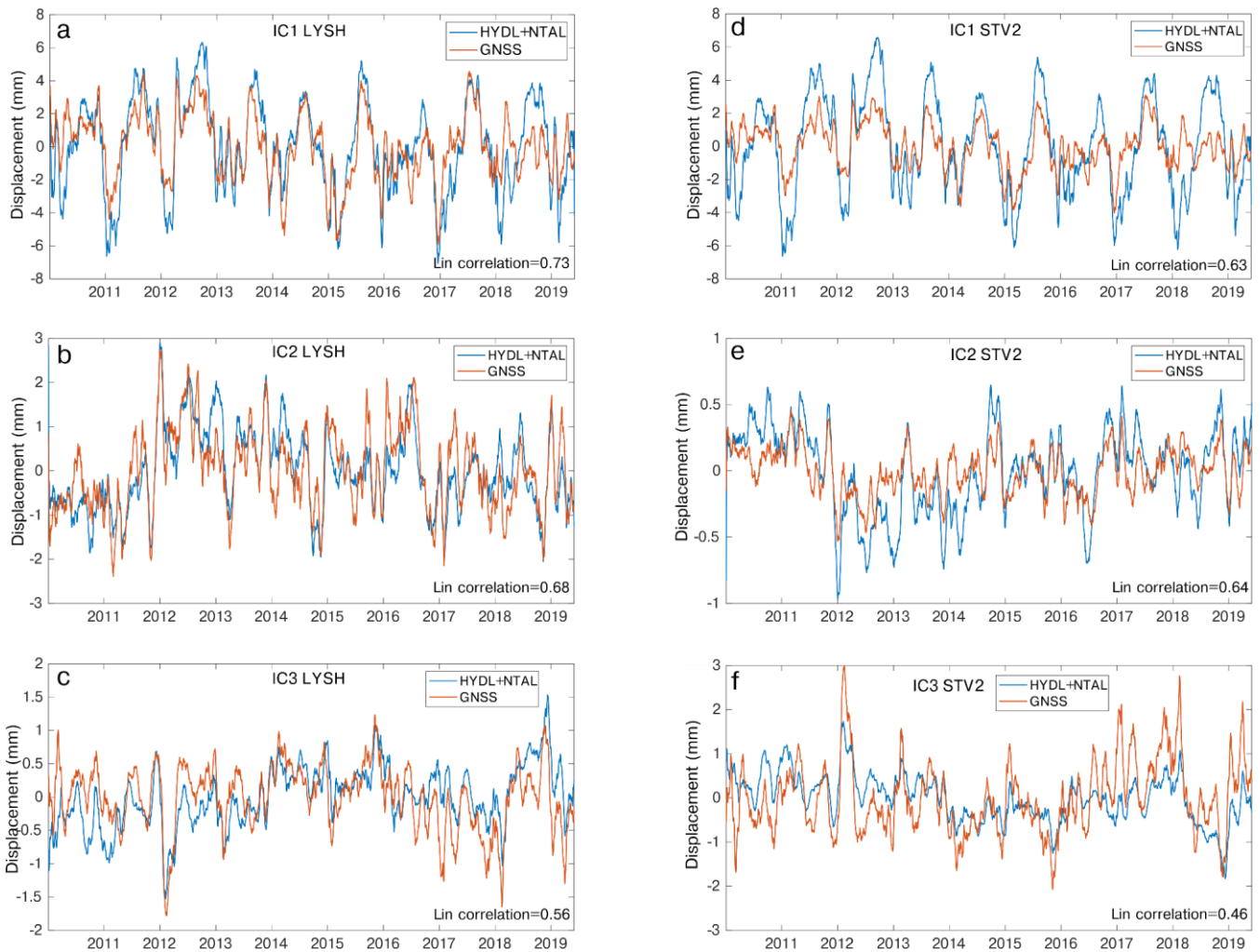
377 To summarize, the three common mode signals components of the GNSS decomposition (IC1, IC2, IC3) are likely due to the
378 combined effect of the atmospheric and hydrological loading. Due to the similarity between the spatial response of
379 displacements associated with these two processes, it is possible that the vbICA technique is not able to separate them in the
380 geodetic data; nonetheless, it highlights their spatial variability through IC2 and IC3.

381 Examples of comparison between climate-related displacements reconstructed at two different sites and the GNSS
382 decomposition are shown in Fig. 8.
383



384
385
386
387

Figure 7: Lin correlation coefficients between: a) GNSS-IC1 and NTAL+HYDL_IC1; b) GNSS_IC2 and NTAL+HYDL_IC2; c) GNSS-IC3 and NTAL+HYDL_IC3. Histograms of the correlation coefficients are also reported.



389

390

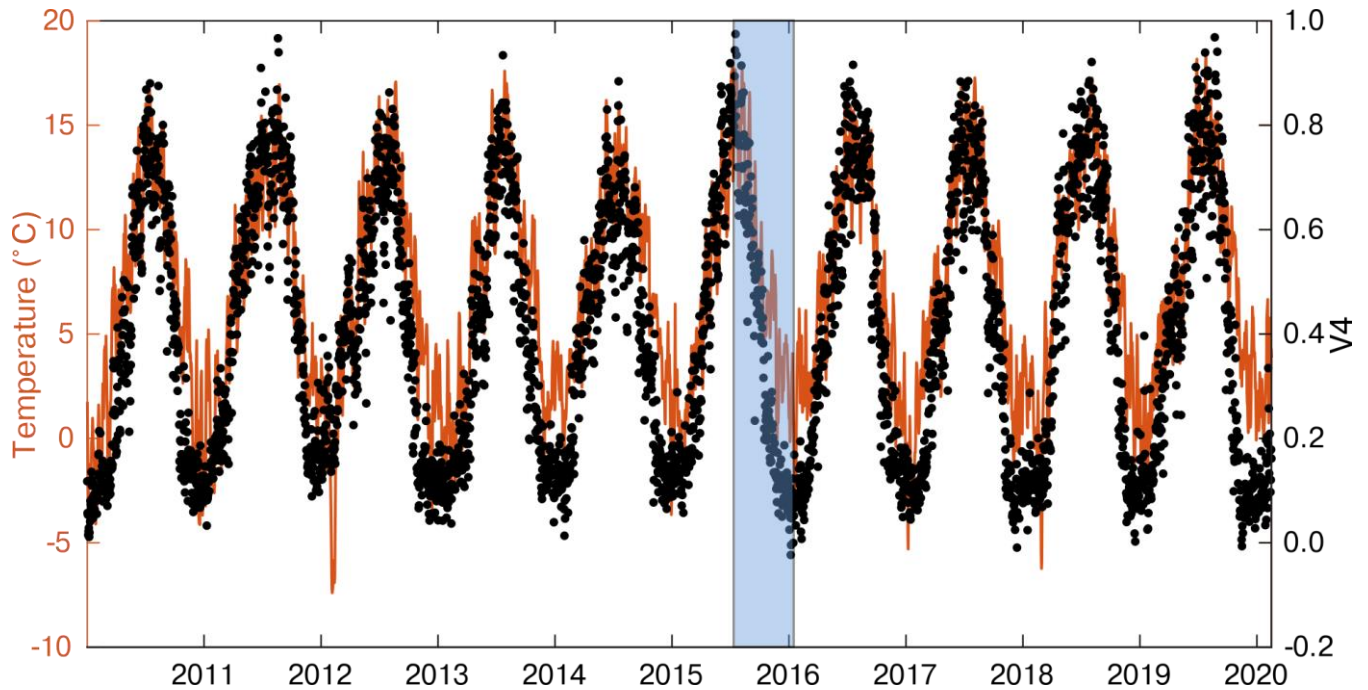
Figure 8: Comparison, at the LYSH (Lon: 18.45°; Lat: 49.55°) site, between the displacements associated with: a) GNSS_IC1 and NTAL+HYDL_IC1; b) GNSS_IC2 and NTAL+HYDL_IC2 ; c) GNSS_IC3 and NTAL+HYDL_IC3. d), e), f) are the same as a), b), c), respectively, for the STV2 (Lon: 6.11°; Lat: 44.57°) site. A 30-days moving average filter is applied to better visualize the data.

393

394

Concerning IC4 of the GNSS decomposition, it describes vertical motions in phase, and very well correlated, with the daily mean temperature of the investigated area (Fig. 9). Temperature data are provided by the E-OBS dataset from the EU-FP6 project UERRA (<https://www.uerra.eu>; Cornes et al., 2018). From the point of view of the spatial distribution of this component, most of the stations located in the mountain chain subside when the temperature increases, while the remaining stations uplift as the temperature increases. Figure S15 shows some cross sections plotting the maximum vertical displacements associated with IC4 together with topography, showing this peculiar spatial pattern.

399



400
 401 **Figure 9: Comparison between the daily mean temperature of the study area (orange) and the temporal evolution of IC4 (black**
 402 **dots). The shaded area represents the time interval associated with the maximum displacements shown in Fig. S15.**

403 4.3 Vertical ground motion rates and noise analysis

404 We show the impact of the filtering on GNSS displacement rates and uncertainties, where the filtered time-series are the result
 405 of subtracting from the IGB14-time series the combined displacement associated ~~ones~~ with the first 4 ICs discussed in Sect.
 406 4.1, which represent the combined effect of the temperature and of the atmospheric and hydrological loading. We refer to these
 407 corrected time series as ICs filtered time series.

408 Velocities and uncertainties are estimated using the Hector software (Bos et al., 2013), assuming a priori noise models. Noise
 409 is commonly described as a power-law process

$$410 P_x(f) = P_0(f/f_0)^k \quad (2)$$

411 where P_x is the power spectrum; f the temporal frequency; P_0 and f_0 are constants; k is the spectral index and it indicates the
 412 noise type.

413 If the power spectrum is flat (i.e., all frequencies have the same power), then the errors are statistically uncorrelated from one
 414 another, the spectral index is zero and the noise is called “white”. Otherwise the noise shows a dependency with the frequency
 415 content, and it is referred to as “colored”. In GNSS time series it has been typically observed the presence of noise with a
 416 power spectrum reduced at high frequencies, with the most popular models being a mix of random walk or “red” noise ($k = -$
 417 2) and flicker or “pink” noise ($k = -1$). Red noise is typically associated with station-dependent effects, while pink noise can
 418 be associated with mismodeling in GNSS satellites orbits, Earth Orientation Parameters (Klos et al., 2018) and spatially-

419 correlated large-scale processes of atmospheric or hydrospheric origin (Bogusz and Klos, 2016). Flicker plus white noise
420 model is commonly used in the analysis of GNSS time-series (e.g., Ghasemi Khalkhali et al., 2021 and references therein).
421 In order to select the best noise model for the input time series, we test different combinations of noise models, choosing the
422 one with the lowest value of the Akaike Information Criterion (AIC) and of the Bayesian Information Criterion (BIC). In
423 particular we consider:

- 424 - Flicker + white noise;
- 425 - A general power-law (k not assigned) + white noise (PL+WN);
- 426 - Flicker + Random walk + white noise.

427

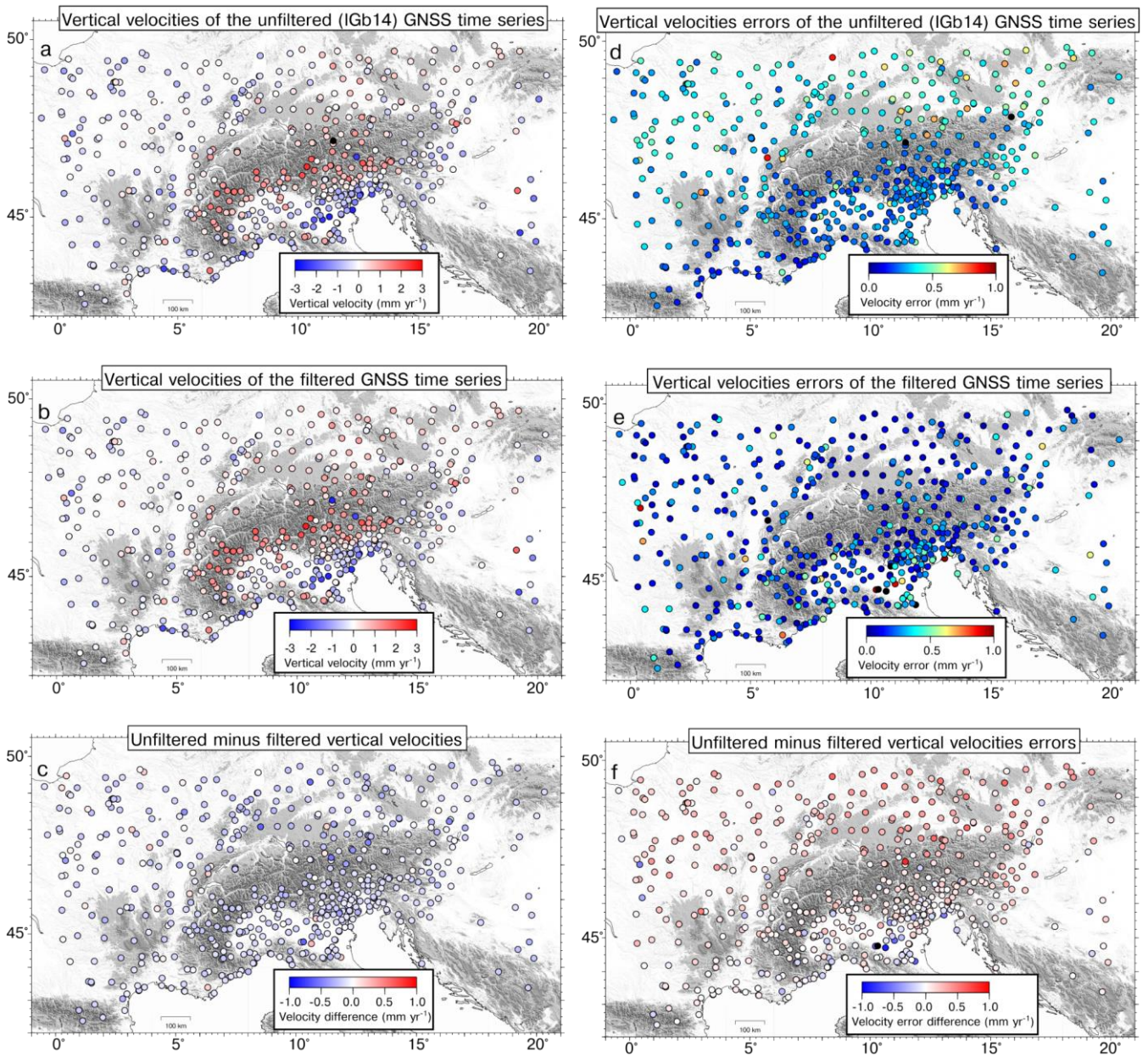
428 Following the AIC and BIC criteria, the preferred noise model is PL+WN, where the parameters of the noise model (i.e., the
429 spectral index k) are estimated by the software using the Maximum Likelihood Estimation (MLE) method. MLE is also used
430 to estimate the station's rates and the associated uncertainties.

431 We then compare the vertical velocities, and their uncertainties, obtained before and after ICs filtering (Fig. 10). Although
432 annual and semi-annual signals are often included in the time series modeling, the displacements associated with the first four
433 ICs already contain these seasonal terms (Fig. 3). Consequently, the ICs filtered time series are modeled only with the linear
434 trend plus temporal correlated noise, while in the unfiltered time series modeling annual and semi-annual terms are also
435 included.

436 Fig. 11a shows histograms representing the differences in the vertical velocity estimates obtained from filtered and unfiltered
437 time-series. The differences are spatially quite homogeneous and of the order of tenths of mm yr^{-1} , with a median value of -
438 0.15 mm yr^{-1} . The velocity differences are almost entirely caused by the displacements associated with IC1, which have a
439 median rate of -0.12 mm yr^{-1} .

440 Concerning the uncertainties associated with the vertical velocity, the impact from ICs filtering is much more important (Fig.
441 10, f and Fig. S17): the initial median error is 0.30 mm yr^{-1} , the final 0.17 mm yr^{-1} .

442



443

444

Figure 10: a) Vertical velocities from the unfiltered GNSS time-series; b) vertical velocities from ICs filtered time series, obtained after subtracting the displacements associated with the first four ICs; c) difference between the velocities of panel a) minus velocities of panel b). d), e), f), same as a), b), c), but showing the error associated with the vertical velocities.

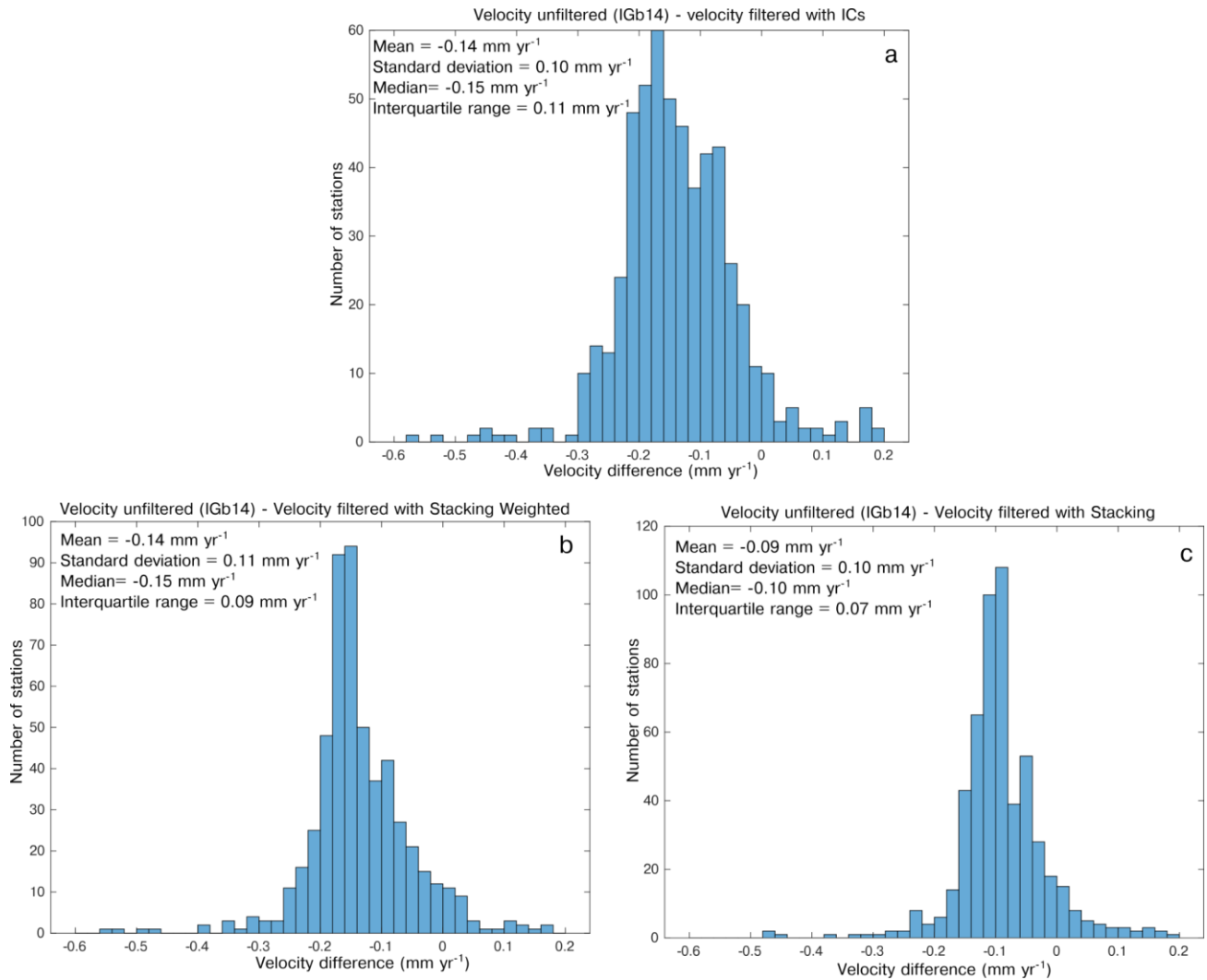
447

448

449

450

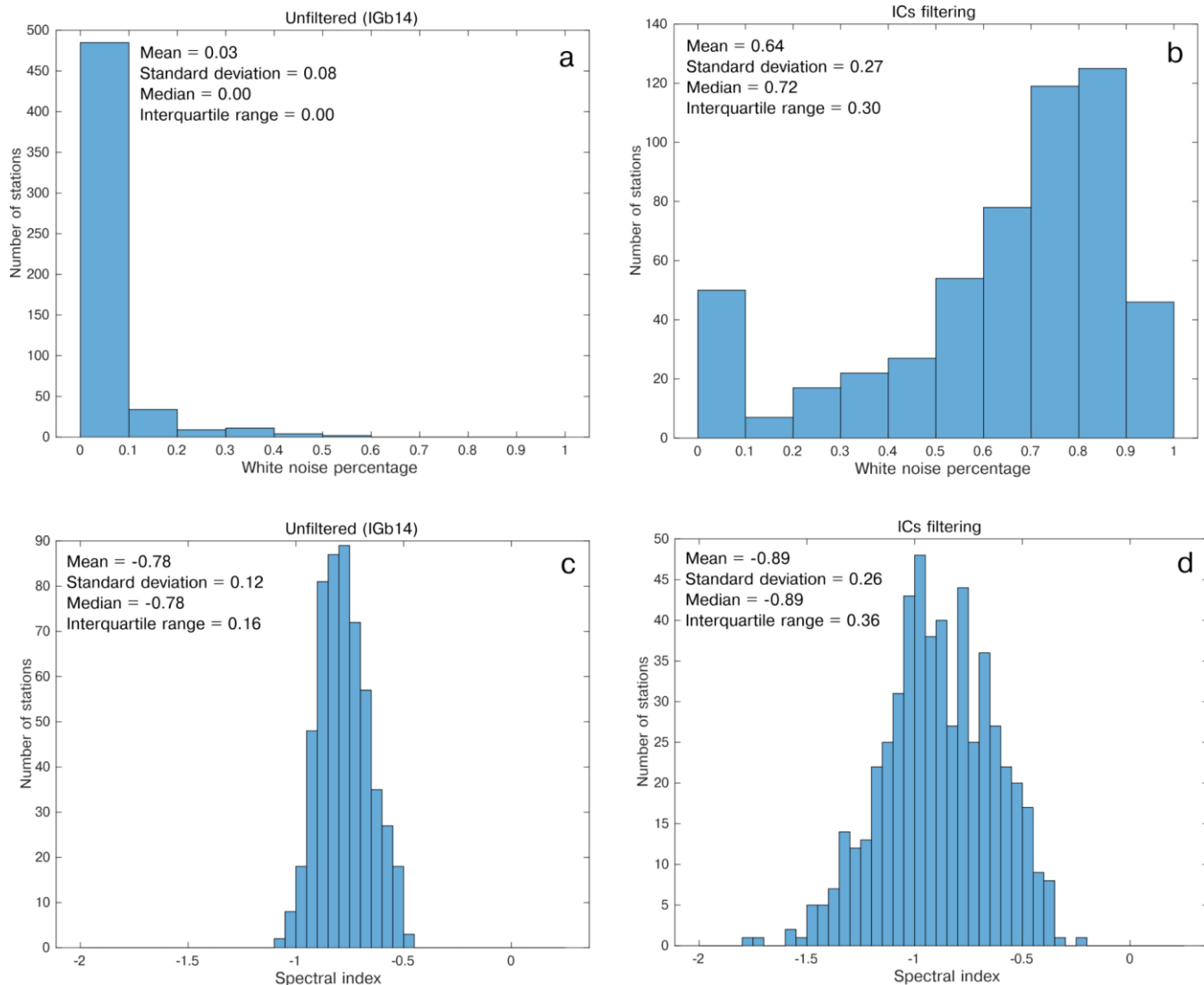
451
452
453
454



455
456
457
458

Figure 11: Histogram of the difference between the velocity of the unfiltered time-series and the filtered ones using: a) the displacements associated with the first 4 ICs; b) the Weighted Stacking Filtering Method; c) the Stacking Filtering Method.

459 The ICs filtering also has a strong impact on the noise characteristics. In fact, while in the unfiltered time series the percentage
460 of white noise of the PL+WN model is negligible in most of the stations, it becomes dominant in the filtered ones (Fig. 12).
461 This indicates that a large portion of the power-law noise is associated with the displacements described by the first 4 ICs, i.e.
462 the atmospheric and hydrological loading and temperature-related processes.



463
 464 **Figure 12: Histograms of: (a) white noise percentage in the unfiltered time-series and (b) filtered time-series. (c), (d) same as (a) and**
 465 **(b) for the spectral index. The filtering is done by subtracting the displacements associated with the first 4 ICs.**

466 **5 Discussion**

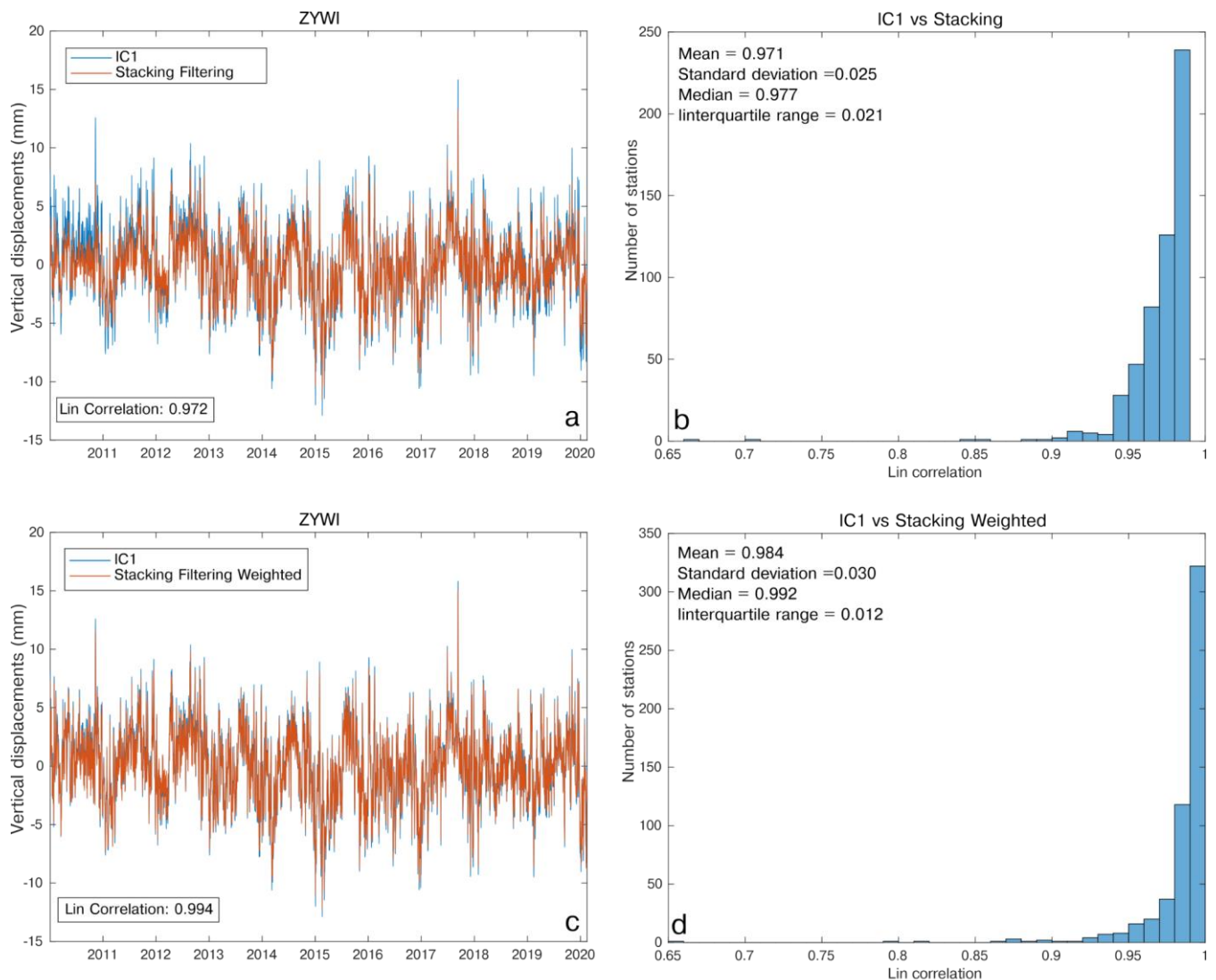
467 **5.1 Displacement time series filtering**

468 Our goal is to estimate the vertical velocity of the GNSS stations associated with long-term geodynamic and tectonic processes,
 469 then we seek to remove signals associated with meteo-climatic processes. Instead of subtracting from the IGB14-time series
 470 the modeled displacements, such as those made available through loading services like GFZ, we prefer to subtract the
 471 displacements associated with the ICs. This approach minimizes biases due to the mismatch between the actual signal caused

472 by atmospheric and hydrological loading and the modeled ones. Larochelle et al. (2018) reached similar conclusions by
473 comparing GRACE measurements and the results from ICA decompositions of GNSS displacements, which resulted to be
474 more accurate in correcting GNSS from seasonal displacements than removing GRACE displacements, which smooth local
475 effects in the data acquisition and processing. In order to support the approach followed, we estimated the scatter of the GNSS
476 displacement time series by computing the mean standard deviation of 1) the time series given as input to vbICA (IGb14-time
477 series), 2) the IGB14-time series minus the combined displacement associated with the first 3 ICs and 3) the IGB14-time series
478 minus the displacements due to HYDL+NTAL from GFZ models. The resulting standard deviation is 5.32, 4.10 and 4.73,
479 respectively. This demonstrates that removing the displacement associated with the first four ICs is more effective in reducing
480 the scatter than removing the HYDL+NTAL contribution.

481 Considering that the stacking methods are widely used to estimate and remove CMS and CME from GNSS time-series (see
482 Sect. 2), we compare the results obtained adopting the SFM and WSFM methods with the output of vbICA, in particular with
483 the displacements associated with IC1 (Fig. 3a), which is clearly a CMS, given its homogeneity in its spatial response. CMS
484 with the stacking methods is estimated using the GNSS_TS_NRS code (He et al., 2020) and it is compared with the
485 displacements associated with IC1 estimating the Lin correlation coefficient. Figure 13 shows that there is an almost-perfect
486 agreement between the IC1-related displacements and the CMS extracted with both stacking methods, suggesting that even
487 simple approaches, such as SFM and WSFM, perform well at the scale of the study area.

488 We also estimate the vertical velocities of the GNSS stations after filtering the CMS using the two stacking methods. The rate
489 differences between unfiltered and filtered time series have a median value of -0.15 and -0.10 mm yr^{-1} , using the WSFM and
490 SFM, respectively (Fig. 11b, c). These values are close to the rates associated with IC1 displacements (median = -0.12 mm yr^{-1}),
491 which are the primary cause of the velocity difference obtained from IGB14 and ICs filtered time-series, suggesting that the
492 rate difference does not strongly depend on the filtering method adopted.
493 As already shown in Sect. 4.3, the errors associated with the velocities of the unfiltered and filtered time series, which have
494 median values of 0.30 and 0.17 mm yr^{-1} , respectively, have about the same value of the velocity difference between filtered
495 and unfiltered time series. It follows that the velocity differences are, from a statistical point of view, barely significant.
496 Nonetheless, it is worth considering that, according to the LSDM-based model, the displacements resulting from the combined
497 effect of hydrological and atmospheric loading have a negative rate (median = -0.11 mm yr^{-1} ; Fig. S16c) in agreement with
498 the rate observed for IC1 (V1 in Fig. 3), suggesting that environmental loading may cause a small subsidence, at least in the
499 observed time-span, which is captured by IC1. However, the rates of the displacements due to hydrological loading are model-
500 dependent: according to LSDM, they show a negative linear trend (Fig. S16b), as opposed to what is observed using the EOST
501 model (Fig. S16e). As a result, the rates of the displacements due to atmospheric + hydrological loading computed using the
502 EOST model are not in agreement with the rates of the IC1 displacements. This is most likely a consequence of the differences
503 in modeling the hydrological loading-induced displacements; in particular, the EOST model takes into account only water
504 stored as snow and soil moisture, whereas the LSDM model also includes the contribution of rivers, lakes and wetlands.



505

506 **Figure 13: Comparison between the displacement associated with IC1 at the ZYWI site and the CME estimated with**
 507 **the Stacking Filtering Method (a) and the Weighted Stacking Filtering Method (c). We also show the histogram**
 508 **representing the Lin correlation between the displacements associated with the IC1 and the CME estimated with the**
 509 **Stacking Filtering Method (b) and the Weighted Stacking Filtering Method (d) at each site. We point out that the CME**
 510 **computed with the aforementioned methods is, by definition, the same at each station; whereas the displacements**
 511 **associated with IC1 have the same temporal evolution but (slightly) different amplitudes. We plot the station ZYWI as**
 512 **an example.**

513

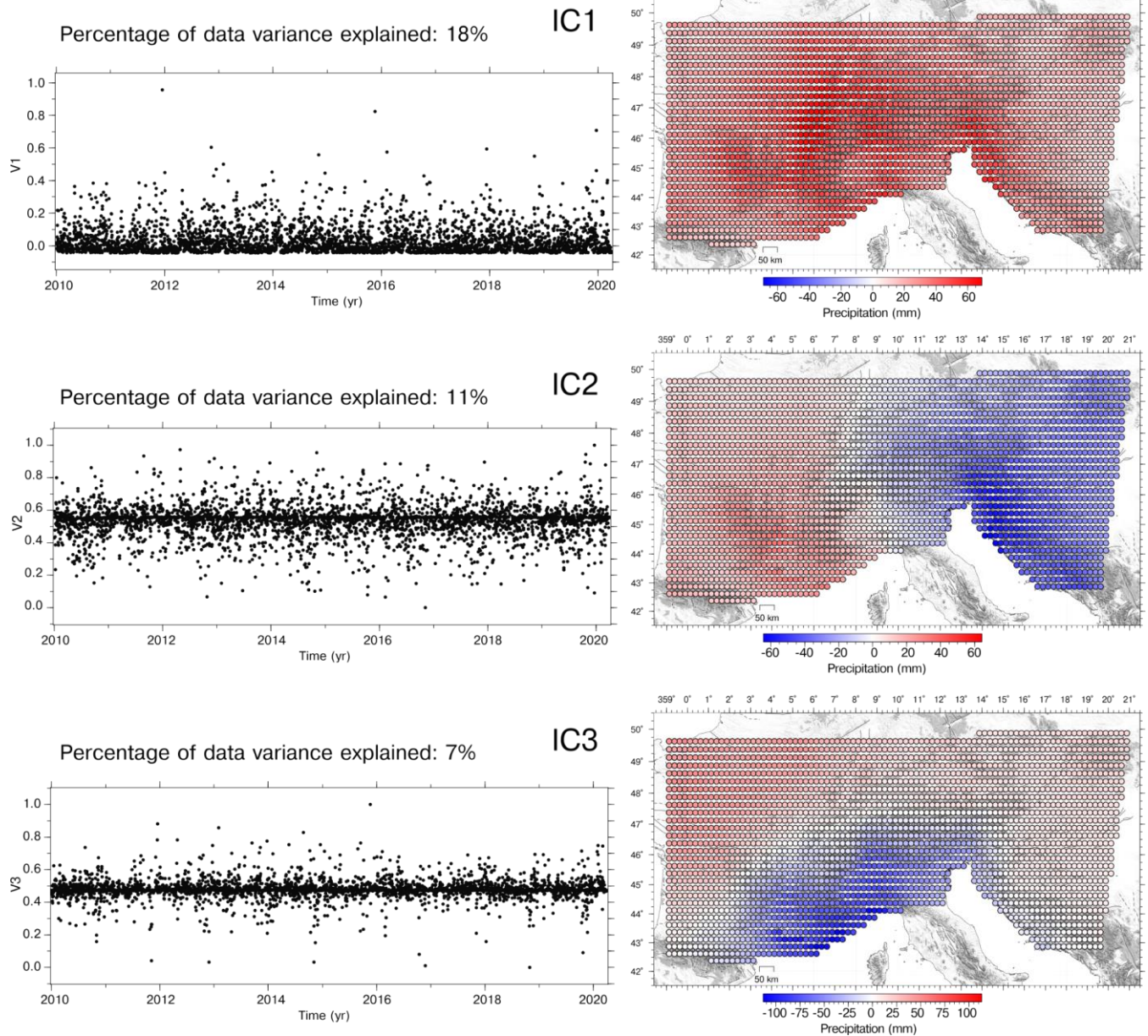
514 The stacking methods used to estimate the CMS are easier and faster to implement than the vbICA analysis. Depending on the
 515 research target, these common mode signals might be worth removing, in order to obtain a more precise, and eventually

516 accurate, estimation of the GNSS linear velocities or retained to study, for example, seasonal deformation. Multivariate
517 statistics and/or source separation algorithms applied to ground displacement time-series allow one to extract and interpret
518 them in terms of the physics behind them, through a comparison with other displacement datasets or models. Furthermore,
519 time series can be filtered not only from CMS, but also from signals associated with spatially uncorrelated processes, as we
520 did in Sect. 4.3 estimating the vertical velocities filtered from non-tectonic processes related to the first four ICs.
521 In Sect. 4.3 we also show that the colored noise in the time series is significantly reduced by the ICs filtering. This result is in
522 agreement with the results of recent studies conducted in other regions, such as Antarctica (Li et al., 2019) and China (Yuan
523 et al., 2018). Both studies show that ICA or PCA filtering of GNSS time series suppress the colored noise amplitudes but have
524 little influence on the amplitude of the white noise. Furthermore, Klos et al. (2021) analyzes the effect of atmospheric loading
525 on the noise of GNSS stations in the European plate, finding that the noise is whitened when NTAL contribution is removed.
526 The description of atmospheric processes at the scale of the Alps can be seen as small scale when compared, for example, to
527 the circulation in the northern hemisphere. Small scale processes are usually interpreted as noise, but they may affect the large-
528 scale dynamics (e.g., Faranda et al., 2017). It follows that these small scale processes should be represented with an appropriate
529 stochastic formulation. Since the CMS are typically characterized by PL+WN noise, the link that we find between CMS and
530 atmospheric and hydrological signals could provide a hint on the type of noise that is more suitable to describe such small
531 scale perturbations when modeling the large-scale dynamics of the atmosphere.

532 **5.2 ICs interpretation**

533 Our analysis supports the interpretation that the displacements associated with IC1, IC2 and IC3 are likely due to the combined
534 effect of the hydrological and atmospheric loading, whose spatial responses are not homogeneous over the study area. In
535 support of this interpretation we can refer to Brunetti et al. (2006), who applied a PCA to precipitation data in the great Alpine
536 area. They highlighted the presence of N-S and E-W gradients in the spatial response of meteo-climating forcing processes.
537 The authors suggest that the main cause of the spatial and temporal variability of the precipitation is the North Atlantic
538 Oscillation (NAO), which also causes fluctuation of the atmospheric pressure (Vicente-Serrano and López-Moreno, 2008). It
539 is then likely that weather regimes like the NAO and the Atlantic Ridge, influence both NTAL and HYDL, which is mainly
540 forced by precipitation, so that the spatial patterns of the ICs associated with atmospheric and hydrological loading are the
541 same of NAO (N-S) and Atlantic Ridge (E-W).
542 The vbICA algorithm is not able to separate NTAL and HYDL because they are not independent from a mathematical point
543 of view. This emerges also from the recent work by Tan et al. (2022), who performed an ICA on GNSS time series of the
544 Yunnan Province of China and interpreted IC1 as the average effects of the joint patterns from soil moisture and atmospheric-
545 induced annual surface deformations. Let us consider for example the case of IC2_NTAL and IC2_HYDL. They have two
546 different temporal evolutions ($V2_NTAL$ and $V2_HYDL$); but the spatial distributions ($U2_NTAL$ and $U2_HYDL$) have the
547 same pattern, i.e. they only differ for a weighting factor k . Then, we can write $U2_NTAL = k * U2_HYDL$.
548 The displacement d resulting from the combined effect of IC2_NTAL and IC2_HYDL is then:

549 $d = IC2_NTAL + IC2_HYDL = U2_NTAL * V2_NTAL + U2_HYDL * V2_HYDL = U2_HYDL * (k * V2_NTAL + V2_HYDL)$.
550 As a result, the displacement due to $IC2_NTAL + IC2_HYDL$ is identified by a single spatial distribution $U2_HYDL$ and a
551 temporal evolution $k * V2_NTAL + V2_HYDL$. Then, if we do not make any prior assumptions about $V2_NTAL$ and
552 $V2_HYDL$, it is not possible to separate $IC2_NTAL$ and $IC2_HYDL$ from a statistical point of view.
553 In Sect. 4.2 we show that not only $IC2_NTAL$ and $IC2_HYDL$ have very similar spatial patterns, but also $IC1_NTAL$ and
554 $IC1_HYDL$, $IC3_NTAL$ and $IC3_HYDL$ have similar spatial responses. Then, the GNSS time-series decomposition in the
555 Alpine area does not allow separating the effect of the hydrological loading from the atmospheric loading with an ICA
556 approach.
557 We also performed a vbICA analysis on precipitation data (RAIN) recorded over the study region, using 3 ICs (Fig. 14). The
558 spatial pattern of the ICs is analogous to the ones associated with $NTAL$ and $HYDL$ (Fig. 4 and Fig. 5).
559



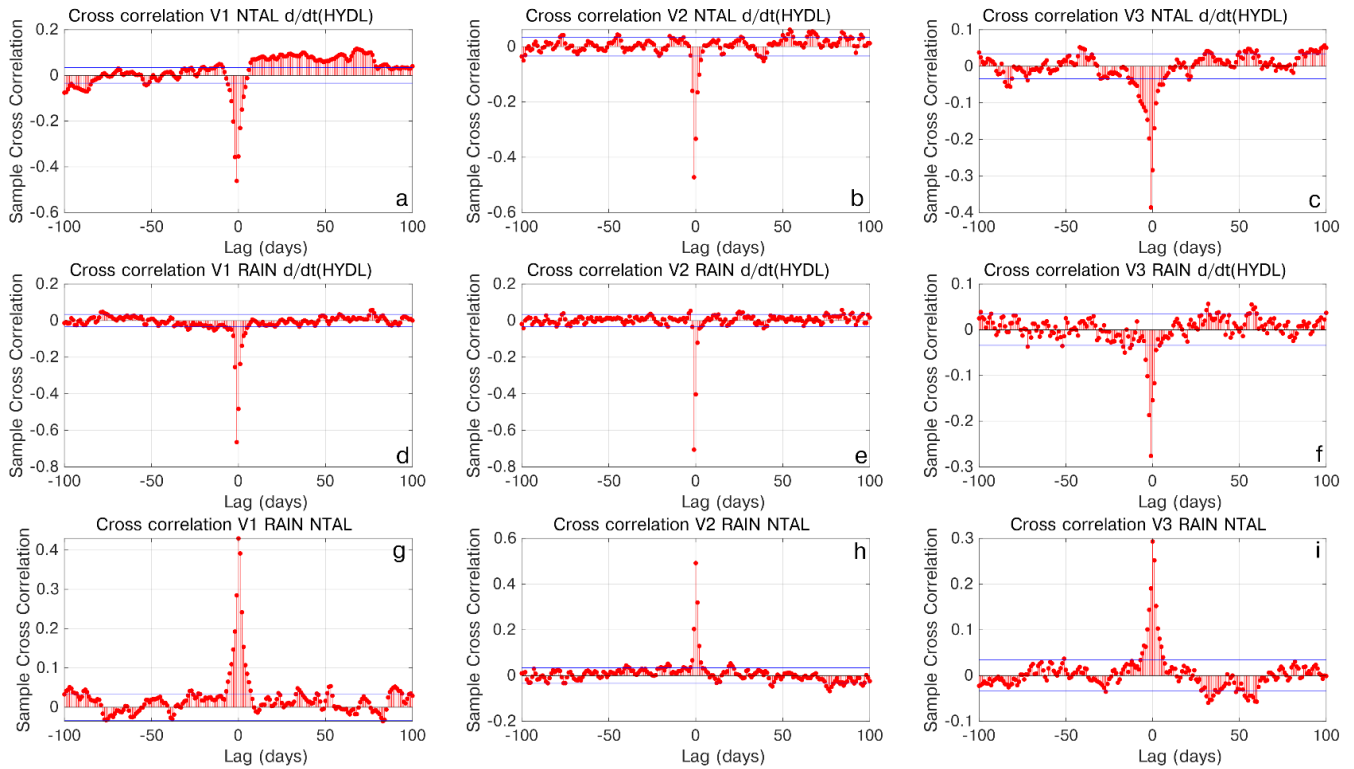
560
561
562

Figure 14: IC1, IC2 and IC3 of the RAIN decomposition.

563 This supports the hypothesis that precipitation, atmospheric pressure, hydrological loading and ground displacement are
564 somehow interconnected and characterized by a common climate-related forcing, whose characteristics of spatial variability
565 are described by the NAO and Atlantic Ridge weather regimes.

566 We point out that HYDL, NTAL and GNSS are models or measurements of vertical displacements, which are positive when
567 upward and negative when downward; while RAIN is the amount of fallen rain per unit area.

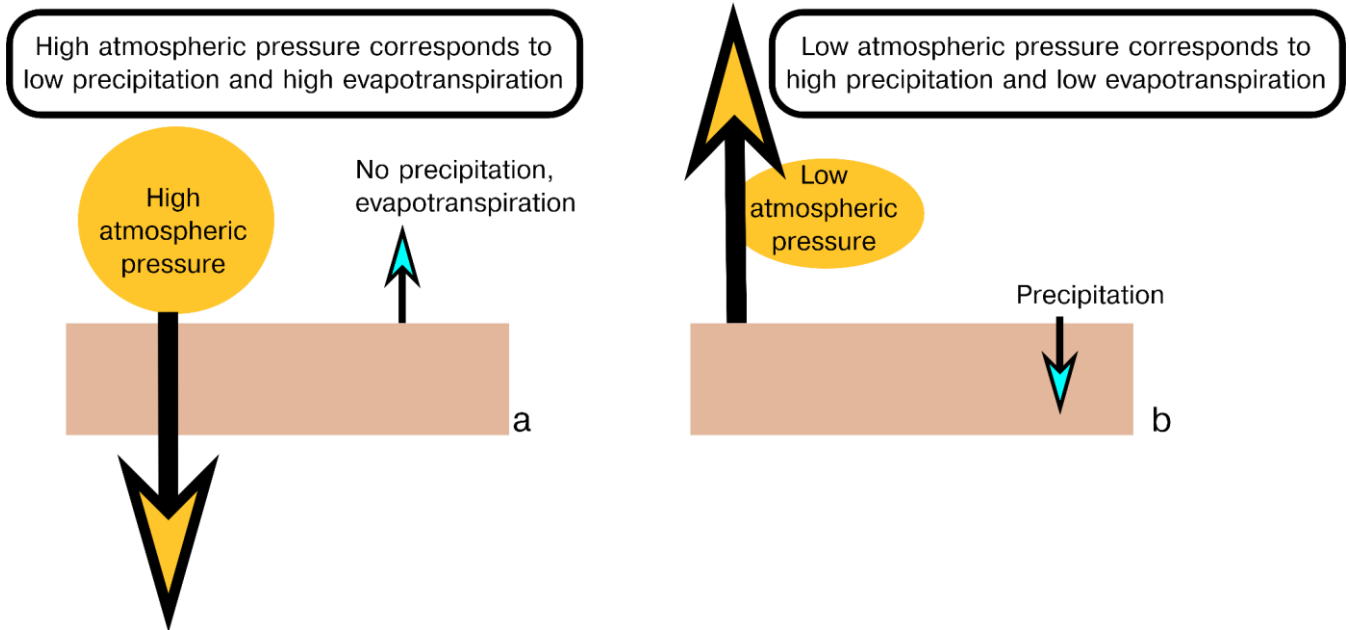
568 Let us consider for the sake of simplicity the IC1 case, but what we are going to discuss holds true also for IC2 and IC3.
 569 The temporal evolution of NTAL_IC1 (NTAL_V1) is correlated with the temporal evolution of RAIN_IC1 (RAIN_V1, Fig.
 570 15g-i) and anti-correlated with the time derivative of the temporal evolution of HYDL_IC1 (HYDL_V1, Fig. 15a-c).
 571 HYDL_V1 is also highly anti-correlated with RAIN_IC1 (Fig. 15d-f).



572 **Figure 15: Cross correlation between:**
 573 **a) the temporal evolution of the IC1 of the NTAL decomposition and the time derivative of the temporal evolution of the IC1 obtained**
 574 **by decomposing HYDL; b) same as a), but considering IC2; c) same as a), but considering IC3;**
 575 **d) the temporal evolution of the IC1 of the precipitation data decomposition and the time derivative of the temporal evolution of the**
 576 **IC1 obtained by decomposing HYDL; e) same as d), but considering IC2; f) same as d), but considering IC3;**
 577 **g) the temporal evolution of the IC1 of the NTAL decomposition and the temporal evolution of the IC1 of the precipitation data**
 578 **decomposition; h) same as g), but considering IC2; i) same as g), but considering IC3.**

580
 581 Our interpretation of the correlations discussed above, schematically represented in Fig. 16, is the following: when the weather
 582 goes from a low pressure to a high pressure regime, the increasing pressure causes a downward displacement of the ground
 583 (Fig. S8). Anyway, low pressure regimes are often associated with precipitation, and that is why IC1_RAIN and IC1_NTAL
 584 are correlated. It follows that when we go from high pressure to low pressure conditions, the ground motion, if we assume a
 585 pure elastic process, is affected by two forces acting in opposite directions: the decreasing atmospheric pressure induces uplift,

586 while the precipitation load causes downward motion. Rain also affects hydrological loading, increasing it and causing a
587 downward ground motion. As a consequence, the temporal derivative of HYDL_IC1, which is more sensitive to small but fast
588 variation of hydrological loading than HYDL itself, is negative and anti-correlated with IC1_RAIN.
589



590
591 **Figure 16: Schematic representation of the ground vertical displacement due to elastic deformation during high pressure (a) and**
592 **low pressure (b) conditions. Yellow arrows reflect displacements associated with atmospheric pressure, blue arrows reflect**
593 **displacements associated with precipitation and evapotranspiration.**

594
595 Atmospheric pressure variations happen at fast temporal scales, then the switch from high to low pressure conditions (and vice
596 versa) can happen in a few days and cause quite large (centimetric) ground vertical displacements. Hydrological loading acts
597 at longer timescales and there are several factors to consider besides precipitation, in particular the temperature, which causes
598 evapotranspiration. Nonetheless, computing the time derivative of the hydrological loading allows to detect “fast” variations
599 due to the change of the atmospheric pressure and the precipitation events often associated with it.

600 The interpretation of IC4 is less straightforward and the pattern we see in the Alps (Figure S.15) is not easy to explain. Air
601 temperature increase can induce both positive and negative vertical displacements. One possible mechanism to explain
602 negative vertical displacements associated with temperature increase is that in the alpine valleys the water content increases
603 as the temperature increases because of the snow and ice melting. It follows that in those areas the elastic response to
604 hydrological load is higher during summertime than winter, as observed by Capodaglio et al. (2017), so that negative vertical
605 displacements are measured when the temperature increases. Then, it is not surprising that in the alpine valleys the stations
606 affected by large IC4-related displacements move downward as temperature increases. This may be an example of a small-

607 scale hydrological process that is likely badly reproduced by the HYDL displacement dataset, which does not have a spatial
608 resolution fine enough to represent hydrological loading displacements at the scale of the alpine valleys. Other site-dependent
609 processes that can potentially induce uplift during winter are the ice formation, and subsequent melting, in the antenna and
610 antenna mount (Koulali and Clarke, 2020) and soil freezing (Beck et al., 2015).

611 Conversely, positive vertical displacements as the temperature increases can be caused by monument/bedrock thermal
612 expansion and the drying of the soil, because of the reduction of the hydrological load. While HYDL takes into account the
613 drying of the soil, we cannot exclude that some local, unmodeled, environmental conditions can amplify this effect at some
614 sites. This might explain why most of the sites affected by uplift during temperature increases are located in plain areas, like
615 the northern sector of the Paris Basin and in the Po plain, instead of the mountainous ones.
616 The relation between IC4 and local processes is also suggested by the heterogeneity of this signal in terms of its spatial
617 distribution, sign, amplitude and relevance in explaining the data variance. In fact, while ~50% of the stations have $U_4 < 2\text{mm}$
618 (Fig. S3d) and explain $< 1\%$ of the data variance, meaning that IC4 is almost useless to reproduce the original data, there is a
619 non-negligible number of stations (~10%) explaining $> 10\%$ of the data variance and with $U_4 > 6\text{mm}$.
620 In the introduction we mentioned the effects of the non-tidal ocean loading on the vertical displacements and both LSDM-
621 based and EOST models provide estimation of them. In the study region, this process induces displacements that are
622 significantly smaller than both atmospheric and hydrological loading, due to the distance from the oceans of the study area, so
623 we do not take it into account. According to the estimation of the LSDM-based model, the maximum amplitude of the spatial
624 mean over the study region of the displacements associated with it is 4.3 mm; while the maximum amplitude of the
625 displacements associated with atmospheric and hydrological loading are 23.8 mm and 12.2 mm, respectively. Figure S5
626 provides a comparison of the spatial mean of the displacements associated with the three deformation mechanisms.

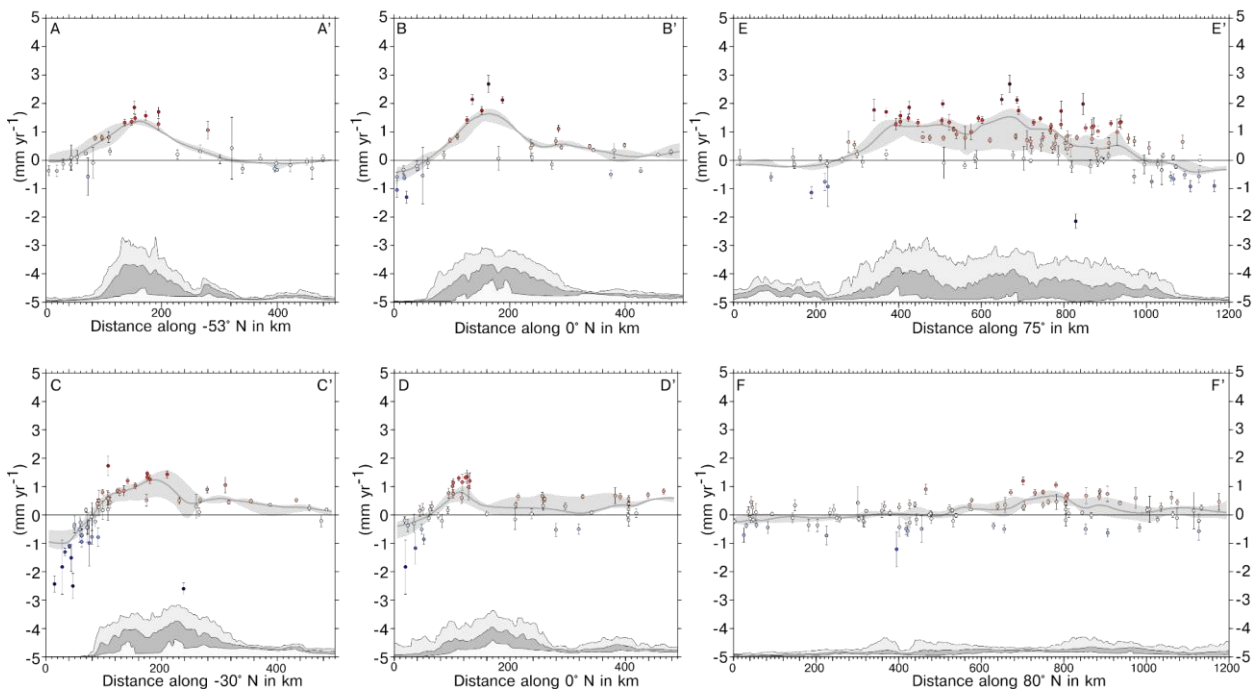
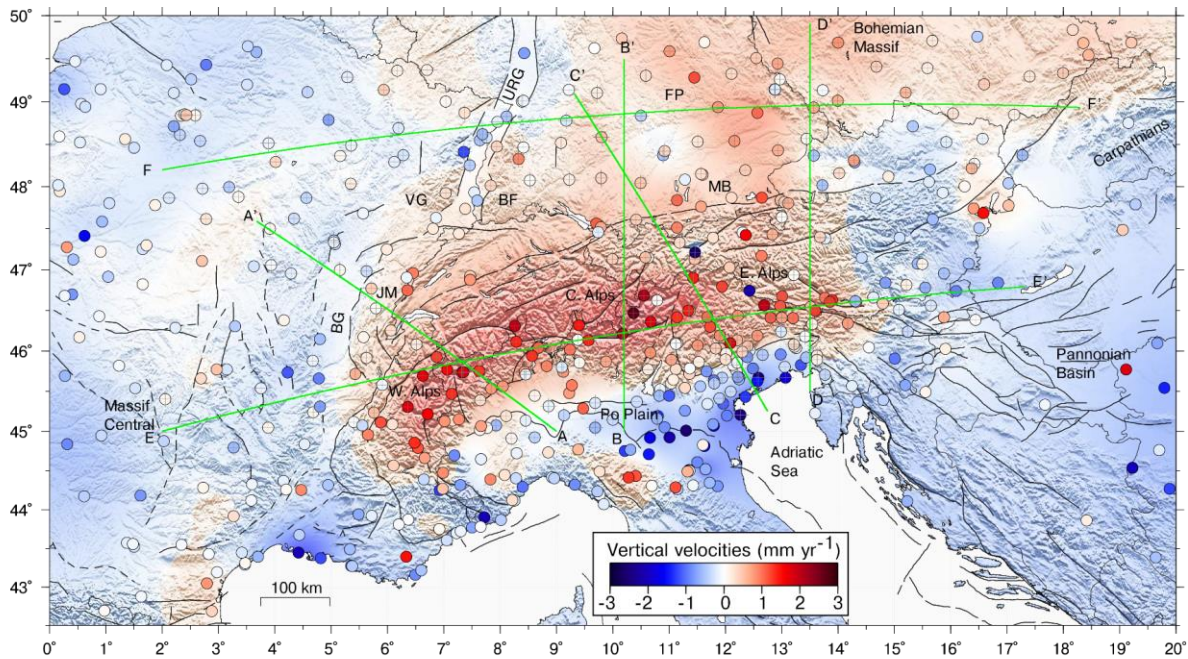
627 **5.3 Vertical velocity gradients across the Alps**

628 The vertical velocity field of the IGB14-time series and of the IGB14-time series with the contribution of the first 4 ICs removed
629 (ICs filtered) do not differ much in terms of uplift/subsidence patterns (see Fig. 11), both showing the belt of continuous uplift,
630 of the order of $1\text{-}2\text{ mm yr}^{-1}$, along the Alpine mountain chain. As shown in Fig. 11c, the vertical velocities from filtered time-
631 series show barely faster positive rates, mainly as an effect of filtering out hydrological and atmospheric displacements of IC1,
632 as discussed above. Figure 17 shows the continuous vertical velocity field obtained from the discrete values adopting the
633 multiscale, wavelet-based, approach described in Tape et al. (2009), and some vertical velocity and topographic profiles
634 running across the great Alpine area. The same figure obtained using velocities and uncertainties from unfiltered time-series
635 is shown in the Supplementary Information (Fig. S19). Despite the similarity in the velocity patterns, the improvements in
636 both the precision and consistencies of vertical spatial gradients are apparent in cross section view. Profile E-E' in Fig. 17
637 shows positive vertical rates increasing from W to E, with the maximum uplift rates in the central Alps, and the positive
638 correlation with the topography along the chain axis, with decreasing rates toward the east, changing to subsidence east of
639 Lon. $\sim 14.5^\circ\text{ E}$, while entering the Pannonian basin domain. The correlation with topography is also clear in the chain-normal

640 profiles (A-A', B-B', C-C' and D-D'). In the Western and Central Alps (A-A' and B-B') the maximum uplift rates are located
641 in correspondence with the maximum elevation, whereas in the Eastern Alps (C-C' and D-D') the maximum uplift rates are
642 shifted southward. The Eastern Southern Alps is the region where the largest part of the Adria-Eurasia converge is
643 accommodated (1-3 mm yr⁻¹), through active thrust faults and shortening (Serpelloni et al., 2016). Here, maximum uplift rates
644 are likely due to interseismic deformation, and their position, across the belt, is driven by thrust fault geometries, slip-rates and
645 locking depths (Anderlini et al., 2020). Concerning the south Alpine foreland in the Po Plain and Venetian plain, Fig. 17 shows
646 a decrease in the vertical velocities from west to east, with barely positive rates in the western Po Plain and increasing
647 subsidence rates in the northern Adriatic and in the northern Apennines foreland.

648 In the Alpine foreland, positive, sub-mm yr⁻¹, velocities are present in the Jura Mts. and the Molasse basin, but uplift extends
649 further northward in the Black Forest and the Franconian Platform, in southern Germany, and in the southern part of the
650 Bohemian Massif. Overall, in the portion of central Europe investigated in this work, we see two different patterns: prevalent
651 stable to slowly-subsiding sites (< 1 mm yr⁻¹) are present west of the Rhine graben, whereas a prevalence of slowly uplifting
652 sites (< 1 mm yr⁻¹) is present east of it. Profile F-F' in Fig. 17 better highlights this pattern. Across the Upper Rhine Graben,
653 the weak uplift signal in the graben's shoulders, the Vosges Mts and Black Forest, is associated with subsidence of stations
654 located within the graben, according to Henrion et al. (2020). To the east, uplift in the Franconian Platform and the Bohemian
655 Massif is only partially correlated with topography. It is still debated whether uplifted regions across NW Europe attest to
656 lithospheric buckling in front of the Alpine arc or were randomly produced by a swarm of baby plumes. Uplift propagation by
657 interferences with the Western Carpathians and possible mantle processes, as suggested by the positive dynamic and residual
658 topography (Faccenna et al., 2014), may contribute to the observed uplift in the Bohemian Massif.

659 Sternai et al. (2019) investigated the possible relative contribution of different geophysical and geological processes in the
660 actual vertical velocity budget over the Alps, suggesting that the interaction among tectonic and surface mass redistribution
661 processes, rather than an individual forcing, better explain vertical deformation in the Alps. Mey et al. (2016) suggested that
662 ~90% of the present-day uplift of the Alpine belt is due to the melting of the LGM ice cap. While it is difficult to independently
663 constrain the patterns and magnitude of mantle contributions to ongoing Alpine vertical displacements at present, lithospheric
664 adjustment to deglaciation and erosion are by far the most important ongoing process, but other authors suggest that other
665 processes are currently shaping the vertical ground motion pattern. In the western and central Alps, active convergence is
666 inactive or limited, the residual uplift rates, after correction from isostatic contributions, are likely due to deep-seated mantle
667 processes, including for example detachment of the western European slab and dynamic contributions related to sub-
668 lithospheric mantle flow (Chery et al., 2016; Nocquet et al., 2016; Sternai et al., 2019). A tectonic contribution to the ongoing
669 uplift is, instead, more likely in the Eastern Alps, and in particular in the Southeastern Alps, where the Adria-Europe
670 convergence is accommodated. However, Anderlini et al (2020) observed that more accurate glacio isostatic models would be
671 needed when interpreting tectonic contributions to uplift at the edge of ice caps, as in the Eastern Southern Alps.



672

673

674

675

Figure 17: Vertical velocities from filtered time-series (colored circles), continuous velocity field, topographic and swath profiles across the great Alpine area. Each profile (green line) encompasses a 50+50 km swath. BG: Bresse Graben; JM: Jura Mts.; VG: Vosges Mts.; BF: Black Forest; URG: Upper Rhine Graben; FP: Franconian Platform; MB: Molasse Basin.

676 **6 Conclusions**

677 The application of a blind source separation algorithm to vertical displacement time-series obtained from a network of GNSS
678 stations in the Great Alpine Area allows us to identify the main sources of vertical ground deformation. Besides the linear
679 trend, vertical displacements are influenced by: 1) atmospheric pressure loading, 2) hydrological loading and 3) temperature-
680 related processes. The analysis of displacement time series of environmental loading shows that the largest vertical motions
681 are related to the variation of atmospheric pressure, in particular when considering daily/weekly timescales. Seasonal
682 displacements are more clearly associated with hydrological loading and temperature-related processes. However, while
683 deformation associated with temperature is well isolated, we were not able to clearly separate the atmospheric and hydrological
684 loading signals in the GNSS displacement time-series.

685 We use the results of the time-series decomposition to filter the IGB14 time-series and study the effect of removing signals
686 associated with environmental loading and temperature-related processes on the vertical velocities and uncertainties.
687 Removing these signals causes a quite uniform, but limited ($\sim 0.1 \text{ mm yr}^{-1}$), increase of the velocities, which we interpret as
688 due to the small negative linear trend associated with the atmospheric and hydrological loading-induced displacements. It is
689 worth noting that the procedure used in this work to estimate the station velocities does not allow to distinguish the tectonic
690 velocities from the contribution to the velocity induced by climate-related processes, in particular if the linear trend associated
691 with ATML and/or HYDL time series is large. Furthermore, the filtering almost halves the uncertainties associated with the
692 velocities and changes the noise spectra, increasing the white noise percentage to the detriment of the colored one.

693 Although providing a geological/geophysical explanation for the observed vertical velocity pattern is out of the scope of this
694 work, we can conclude that more precise and accurate vertical velocities, such as the one presented in this work, can be obtained
695 by careful signal detection and filtering. This can help develop better spatially resolved models, aiming at a more effective
696 understanding of the relative contribution of the different ongoing geodynamic and tectonic processes shaping the present-day
697 topography of the Alps.

698 **Code and data availability**

699 The MATLAB code for vbICA decomposition is available from <http://dx.doi.org/10.17632/n92vwbg8zt.1>. Global datasets
700 used for the hydrological, atmospheric and ocean load model are taken from <http://loading.u-strasbg.fr/> (EOST model) and
701 <http://rz-vm115.gfz-potsdam.de:8080/repository/entry/show?entryid=24aacdfe-f9b0-43b7-b4c4-bdbe51b6671b> (LSDM-
702 based model). Temperature data are available on <https://www.ecad.eu/download/ensembles/download.php> and IGB14 GPS
703 time series on <https://doi.pangaea.de/10.1594/PANGAEA.938422>.

704 **Author contribution**

705 F. Pintori conceived and led the paper, E. Serpelloni coordinated the study and analyzed GNSS data, A. Gualandi supervised
706 the vbICA analysis of GNSS displacements. All the authors discussed the content of the paper and shared the writing.

707 **Competing interests**

708 The authors declare that they have no conflict of interest.

709 **Acknowledgements**

710 We thank E. Scoccimarro and M. Zampieri for fruitful suggestions on the interpretation of meteo-climatic data. F. Pintori was
711 supported by the project TRANSIENTI, founded by the Italian Ministry of Education, Universities and Research (MIUR)
712 “Premiale 2014”. Adriano Gualandi is supported by European Research Council Advance Grant 835012 (TECTONIC). This
713 work has been developed in the framework of the project KINDLE, funded by the “Pianeta Dinamico” INGV institutional
714 project. We acknowledge the E-OBS dataset from the EU-FP6 project UERRA (<https://www.uerra.eu>) and the Copernicus
715 Climate Change Service, and the data providers in the ECA&D project (<https://www.ecad.eu>). We are grateful to the many
716 agencies, companies and networks that have made GNSS data available. We specifically thank the following public networks
717 and institutions for raw RINEX data: IGS, EUREF-EPN, AGROS (Serbia), CZEPOS (Czech Republic), GPS-EMILIA
718 ROMAGNA (Italy), InOGS-FREDNET (Italy), Rete GNSS Marussi FVG (Italy), ASI-GEODAF (Italy), GEONAS (Czech
719 Republic), GFZ (Germany), GREF (Germany), Leica-Geosystem HXGN-SmartNeT (Italy), GNSS LIGURIA (Italy), Topcon
720 Positioning Italy NETGEO (Italy), OLGGPS (Austria), RENAG (France), RGP (France), INGV-RING (Italy), SIGNAL
721 (Slovenia), SONEL, SPINGNSS (Italy), STPOS (BZ, Italy), TPOS (TN, Italy), GPS-VENETO (Italy), VESOG (Czech
722 Republic). ORPHEON data were provided to the authors for scientific use in the framework of the GEODATA-INSU-CNRS
723 convention. We acknowledge Echtzeit Positionierung Austria for providing access to the EPOSA data. SAPOS networks are
724 operated by various German States (Landesamt für Digitalisierung, Breitband und Vermessung and Baden-Württemberg).

725 **References**

726 Anderlini, L., Serpelloni, E., Tolomei, C., De Martini, P. M., Pezzo, G., Gualandi, A. and Spada, G.: New insights into active
727 tectonics and seismogenic potential of the Italian Southern Alps from vertical geodetic velocities, , [https://doi.org/10.5194/se-](https://doi.org/10.5194/se-2020-10)
728 2020-10, 2020.

729 Beck, I., Ludwig, R., Bernier, M., Strozzi, T. and Boike, J.: Vertical movements of frost mounds in subarctic permafrost
730 regions analyzed using geodetic survey and satellite interferometry, *Earth Surf. Dynam.*, 3(3), 409–421,
731 <https://doi.org/10.5194/esurf-3-409-2015>, 2015.

732 Bevis, M. and Brown, A.: Trajectory models and reference frames for crustal motion geodesy, *J. Geod.*, 88(3), 283–311,
733 <https://doi.org/10.1007/s00190-013-0685-5>, 2014.

734 Blewitt, G., Hammond, W. and Kreemer, C.: Harnessing the GPS data explosion for interdisciplinary science, *EOS*, 99,
735 <https://doi.org/10.1029/2018EO104623>, 2018.

736 Bogusz, J. and Klos, A.: On the significance of periodic signals in noise analysis of GPS station coordinates time series, *GPS*
737 *Solut.*, 20(4), 655–664, <https://doi.org/10.1007/s10291-015-0478-9>, 2016.

738 Bos, M. S., Fernandes, R. M. S., Williams, S. D. P. and Bastos, L.: Fast error analysis of continuous GNSS observations with
739 missing data, *J. Geod.*, 87(4), 351–360, <https://doi.org/10.1007/s00190-012-0605-0>, 2013.

740 Brunetti, M., Maugeri, M., Nanni, T., Auer, I., Böhm, R. and Schöner, W.: Precipitation variability and changes in the greater
741 Alpine region over the 1800–2003 period, *J. Geophys. Res.*, 111(D11), <https://doi.org/10.1029/2005JD006674>, 2006.

742 Capodaglio, P., Naldi, M. and Simonetto, F.: Hydrogeological characterization throughout deep geophysical investigations in
743 the Verrès plain (Aosta Valley, north-western Italian Alps), *Acque Sott.*, 6(1), <https://doi.org/10.7343/as-2017-262>, 2017.

744 Chery, J., Genti, M. and Vernant, P.: Ice cap melting and low-viscosity crustal root explain the narrow geodetic uplift of the
745 Western Alps, *Geophys. Res. Lett.* 43 (7), 3193–3200, <https://dx.doi.org/10.1002/2016GL067821>, 2016.

746 Ching, K.-E., Hsieh, M.-L., Johnson, K. M., Chen, K.-H., Rau, R.-J., and Yang, M.: Modern vertical deformation rates and
747 mountain building in Taiwan from precise leveling and continuous GPS observations, 2000–2008. *Journal of Geophysical*
748 *Research*, 116, B08406, <https://doi.org/10.1029/2011JB008242>, 2011.

749 Choudrey, R. A.: Variational Methods for Bayesian Independent Component Analysis. Pattern analysis and machine learning
750 - robotics research group, University of Oxford, 2002.

751 Choudrey, R. A. and Roberts, S. J.: Variational mixture of Bayesian independent component analyzers., *Neural Comput.*,
752 15(1), 213–252, <https://doi.org/10.1162/089976603321043766>, 2003.

753 Cornes, R. C., van der Schrier, G., van den Besselaar, E. J. M. and Jones, P. D.: An Ensemble Version of the E-OBS
754 Temperature and Precipitation Data Sets, *J. Geophys. Res. Atmos.*, 123(17), 9391–9409,
755 <https://doi.org/10.1029/2017JD028200>, 2018.

756 Dal Zilio, L., Hetényi, G., Hubbard, J. and Bollinger, L: Building the Himalaya from tectonic to earthquake scales. *Nature*
757 *Reviews Earth & Environment*, 2, 251–268, <https://doi.org/10.1038/s43017-021-00143-1>, 2021.

758 van Dam, T., Collilieux, X., Wuite, J., Altamimi, Z. and Ray, J.: Nontidal ocean loading: amplitudes and potential effects in
759 GPS height time series, *J. Geod.*, 86(11), 1043–1057, <https://doi.org/10.1007/s00190-012-0564-5>, 2012.

760 Dill, R.: Hydrological model LSDM for operational Earth rotation and gravity field variations, Deutsches
761 GeoForschungsZentrum GFZ, <https://doi.org/10.2312/gfz.b103-08095>, 2008.

762 Dill, R. and Dobslaw, H.: Numerical simulations of global-scale high-resolution hydrological crustal deformations, *J. Geophys.*
763 *Res. Solid Earth*, 118(9), 5008–5017, <https://doi.org/10.1002/jgrb.50353>, 2013.

764 Dong, D., Fang, P., Bock, Y., Webb, F., Prawirodirdjo, L., Kedar, S. and Jamason, P.: Spatiotemporal filtering using principal
765 component analysis and Karhunen-Loeve expansion approaches for regional GPS network analysis, *J. Geophys. Res.*, 111(B3),
766 <https://doi.org/10.1029/2005JB003806>, 2006.

767 Faccenna, C., Becker, T. W., Miller, M. S., Serpelloni, E. and Willett, S. D.: Isostasy, dynamic topography, and the elevation
768 of the Apennines of Italy, *Earth and Planetary Science Letters*, 407, 163–174, <https://doi.org/10.1016/j.epsl.2014.09.027>,
769 2014a.

770 Faccenna, C., Becker, T. W., Auer, L., Billi, A., Boschi, L., Brun, J. P., Capitanio, F. A., Funicello, F., Horvath, F., Jolivet,
771 L., Piromallo, C., Royden, L., Rossetti, F. and Serpelloni, E.: Mantle dynamics in the Mediterranean, *Rev. Geophys.*, 52(3),
772 283–332, <https://doi.org/10.1002/2013RG000444>, 2014b.

773 Faranda, D., Sato, Y., Saint-Michel, B., Wiertel, C., Padilla, V., Dubrulle, B. and Daviaud, F.: Stochastic chaos in a turbulent
774 swirling flow., *Phys. Rev. Lett.*, 119(1), 014502, <https://doi.org/10.1103/PhysRevLett.119.014502>, 2017.

775 Fu, Y. and Freymueller, J. T.: Seasonal and long-term vertical deformation in the Nepal Himalaya constrained by GPS and
776 GRACE measurements, *J. Geophys. Res.*, 117(B3), <https://doi.org/10.1029/2011JB008925>, 2012.

777 Fu, Y., Freymueller, J. T. and Jensen, T.: Seasonal hydrological loading in southern Alaska observed by GPS and GRACE,
778 *Geophys. Res. Lett.*, 39(15), <https://doi.org/10.1029/2012GL052453>, 2012.

779 Gegout, P., Boy, J. P., Hinderer, J. and Ferhat, G.: Modeling and Observation of Loading Contribution to Time-Variable GPS
780 Sites Positions, in *Gravity, Geoid and Earth Observation: IAG Commission 2: Gravity Field*, Chania, Crete, Greece, 23-27
781 June 2008, vol. 135, edited by S. P. Mertikas, pp. 651–659, Springer Berlin Heidelberg, Berlin, Heidelberg,
782 https://doi.org/10.1007/978-3-642-10634-7_86, , 2010.

783 Ghasemi Khalkhali, S. A., A. Ardalan, A. and Karimi, R.: A time series analysis of permanent GNSS stations in the northwest
784 network of Iran, *Annals of Geophysics*, 64(2), <https://doi.org/10.4401/ag-8450>, 2021.

785 Gualandi, A. and Liu, Z.: Variational bayesian independent component analysis for insar displacement time-series with
786 application to central california, USA, *J. Geophys. Res. Solid Earth*, 126(4), <https://doi.org/10.1029/2020JB020845>, 2021.

787 Gualandi, A., Serpelloni, E. and Belardinelli, M. E.: Blind source separation problem in GPS time series, *J. Geod.*, 90(4), 323–
788 341, <https://doi.org/10.1007/s00190-015-0875-4>, 2016.

789 Gualandi, A., Nichele, C., Serpelloni, E., Chiaraluce, L., Anderlini, L., Latorre, D., Belardinelli, M. E. and Avouac, J. P.:
790 Aseismic deformation associated with an earthquake swarm in the northern Apennines (Italy), *Geophys. Res. Lett.*, 44(15),
791 7706–7714, <https://doi.org/10.1002/2017GL073687>, 2017a.

792 Gualandi, A., Perfettini, H., Radiguet, M., Cotte, N. and Kostoglodov, V.: GPS deformation related to
793 the *M* 7.3, 2014, Papanao earthquake (Mexico) reveals the aseismic behavior of the Guerrero seismic
794 gap, *Geophys. Res. Lett.*, 44(12), 6039–6047, <https://doi.org/10.1002/2017GL072913>, 2017b.

795 He, M., Shen, W., Pan, Y., Chen, R., Ding, H. and Guo, G.: Temporal-Spatial Surface Seasonal Mass Changes and Vertical
796 Crustal Deformation in South China Block from GPS and GRACE Measurements., *Sensors*, 18(1),
797 <https://doi.org/10.3390/s18010099>, 2017.

798 He, X., Yu, K., Montillet, J.-P., Xiong, C., Lu, T., Zhou, S., Ma, X., Cui, H. and Ming, F.: GNSS-TS-NRS: An Open-Source
799 MATLAB-Based GNSS Time Series Noise Reduction Software, *Remote Sens (Basel)*, 12(21), 3532,
800 <https://doi.org/10.3390/rs12213532>, 2020.

801 Henrion, E., Masson, F., Doubre, C., Ulrich, P. and Meghraoui, M.: Present-day deformation in the Upper Rhine Graben
802 from GNSS data, *Geophysical Journal International*, 223(1), 599–611, <https://doi.org/10.1093/gji/ggaa320>, 2020

803 Herring, T. A., King, R. W., Floyd, M. A., and McClusky, S. C.: Introduction to GAMIT/GLOBK, Release 10.7, 2018.
804 Retrieved from http://geoweb.mit.edu/gg/Intro_GG.pdf

805 Hou, Z., Guo, Z. and Du, J.: Analysis of the regional GNSS coordinate time series by ICA-weighted spatio-temporal filtering,
806 *J. Earth Syst. Sci.*, 128(7), 191, <https://doi.org/10.1007/s12040-019-1214-6>, 2019.

807 Huffman, G.J., Stocker, E.F., Bolvin, D.T., Nelkin, E.J. and Jackson Tan: GPM IMERG Final Precipitation L3 1 day 0.1
808 degree x 0.1 degree V06, Edited by Andrey Savtchenko, Greenbelt, MD, Goddard Earth Sciences Data and Information
809 Services Center (GES DISC), Accessed: [04-27-2022], 10.5067/GPM/IMERGDF/DAY/06, 2019.

810 Hyvärinen, A. and Oja, E.: A Fast Fixed-Point Algorithm for Independent Component Analysis, *Neural Comput.*, 9(7), 1483–
811 1492, <https://doi.org/10.1162/neco.1997.9.7.1483>, 1997.

812 Jiang, W., Ma, J., Li, Z., Zhou, X. and Zhou, B.: Effect of removing the common mode errors on linear regression analysis of
813 noise amplitudes in position time series of a regional GPS network & a case study of GPS stations in Southern California,
814 *Adv. Space Res.*, 61(10), 2521–2530, <https://doi.org/10.1016/j.asr.2018.02.031>, 2018.

815 Klos, A., Olivares, G., Teferle, F. N., Hunegnaw, A. and Bogusz, J.: On the combined effect of periodic signals and colored
816 noise on velocity uncertainties, *GPS Solut.*, 22(1), 1, <https://doi.org/10.1007/s10291-017-0674-x>, 2018.

817 Klos, A., Dobsław, H., Dill, R. and Bogusz, J.: Identifying the sensitivity of GPS to non-tidal loadings at various time
818 resolutions: examining vertical displacements from continental Eurasia, *GPS Solut.*, 25(3), 89, [https://doi.org/10.1007/s10291-](https://doi.org/10.1007/s10291-021-01135-w)
819 021-01135-w, 2021.

820 Kositsky, A. P. and Avouac, J. P.: Inverting geodetic time series with a principal component analysis-based inversion method,
821 *J. Geophys. Res.*, 115(B3), <https://doi.org/10.1029/2009JB006535>, 2010.

- 822 Koulali, A. and Clarke, P. J.: Effect of antenna snow intrusion on vertical GPS position time series in Antarctica, *J. Geod.*,
823 94(10), 101, <https://doi.org/10.1007/s00190-020-01403-6>, 2020.
- 824 Kreemer, C. and Blewitt, G.: Robust estimation of spatially varying common-mode components in GPS time-series, *J. Geod.*,
825 95(1), 13, <https://doi.org/10.1007/s00190-020-01466-5>, 2021.
- 826 Kumar, U., Chao, B. F. and Chang, E. T. Y.: What causes the common-mode error in array GPS displacement fields: case
827 study for taiwan in relation to atmospheric mass loading, *Earth and Space Science*, 7(11),
828 <https://doi.org/10.1029/2020EA001159>, 2020.
- 829 Larochelle, S., Gualandi, A., Chanard, K. and Avouac, J. P.: Identification and extraction of seasonal geodetic signals due to
830 surface load variations, *J. Geophys. Res. Solid Earth*, <https://doi.org/10.1029/2018JB016607>, 2018.
- 831 Li, W., Li, F., Zhang, S., Lei, J., Zhang, Q., Yuan, L.: Spatiotemporal Filtering and Noise Analysis for Regional GNSS Network
832 in Antarctica Using Independent Component Analysis. *Remote Sens (Basel)*, 11(4), 386, <https://doi.org/10.3390/rs11040386>,
833 2019.
- 834 Lin, L. I.: A concordance correlation coefficient to evaluate reproducibility., *Biometrics*, 45(1), 255–268,
835 <https://doi.org/10.2307/2532051>, 1989.
- 836 Liu, B., Dai, W., Peng, W. and Meng, X.: Spatiotemporal analysis of GPS time series in vertical direction using independent
837 component analysis, *Earth Planet. Sp.*, 67(1), 189, <https://doi.org/10.1186/s40623-015-0357-1>, 2015.
- 838 Liu, B., Dai, W. and Liu, N.: Extracting seasonal deformations of the Nepal Himalaya region from vertical GPS position time
839 series using Independent Component Analysis, *Adv. Space Res.*, <https://doi.org/10.1016/j.asr.2017.02.028>, 2017.
- 840 Masson, C., Mazzotti, S. and Vernant, P.: Precision of continuous GPS velocities from statistical analysis of synthetic time
841 series, *Solid Earth*, 10(1), 329–342, <https://doi.org/10.5194/se-10-329-2019>, 2019.
- 842 Mey, J., Scherler, D., Wickert, A. D., Egholm, D. L., Tesauro, M., Schildgen, T. F. and Strecker, M. R.: Glacial isostatic uplift
843 of the European Alps. *Nature Communications*, 7(1), 13382. <https://doi.org/10.1038/ncomms13382>, 2016.
- 844 Ming, F., Yang, Y., Zeng, A. and Zhao, B.: Spatiotemporal filtering for regional GPS network in China using independent
845 component analysis, *J. Geod.*, 91(4), 419–440, <https://doi.org/10.1007/s00190-016-0973-y>, 2017.
- 846 Nikolaidis, R.: Observation of geodetic and seismic deformation with the Global Positioning System, PhD thesis, Univ. of
847 Calif., San Diego, 2002.
- 848 Nocquet, J.-M., Sue, C., Walpersdorf, A., Tran, T., Lenôtre, N., Vernant, P., Cushing, M., Jouanne, F., Masson, F., Baize, S.,
849 Chéry, J., van der Beek, P. A.: Present-day uplift of the western Alps. *Scientific Reports*, 6(1), 28404.
850 <https://doi.org/10.1038/srep28404>, 2016.
- 851 Palano, M., Pezzo, G., Serpelloni, E., Devoti, R., D’Agostino, N., Gandolfi, S., Sparacino, F., Anderlini, L., Poluzzi, L.,

852 Tavasci, L., Macini, P., Pietrantonio, G., Riguzzi, F., Antoncicchi, I., Ciccone, F., Rossi, G., Avallone, A. and Selvaggi, G.:
853 Geopositioning time series from offshore platforms in the Adriatic Sea., *Sci. Data*, 7(1), 373, [https://doi.org/10.1038/s41597-](https://doi.org/10.1038/s41597-020-00705-w)
854 020-00705-w, 2020.

855 Pan, Y., Chen, R., Ding, H., Xu, X., Zheng, G., Shen, W., Xiao, Y. and Li, S.: Common Mode Component and Its Potential
856 Effect on GPS-Inferred Three-Dimensional Crustal Deformations in the Eastern Tibetan Plateau, *Remote Sens (Basel)*, 11(17),
857 1975, <https://doi.org/10.3390/rs11171975>, 2019.

858 Pintori, F., Serpelloni, E., Longuevergne, L., Garcia, A., Faenza, L., D'Alberto, L., Gualandi, A. and Belardinelli, M. E.:
859 Mechanical response of shallow crust to groundwater storage variations: inferences from deformation and seismic observations
860 in the eastern southern alps, italy, *J. Geophys. Res. Solid Earth*, 126(2), <https://doi.org/10.1029/2020JB020586>, 2021.

861 Riddell, A. R., King, M. A. and Watson, C. S.: Present-day vertical land motion of Australia from GPS observations and
862 geophysical models, *J. Geophys. Res. Solid Earth*, <https://doi.org/10.1029/2019JB018034>, 2020.

863 Rodell, M., Houser, P. R., Jambor, U., Gottschalck, J., Mitchell, K., Meng, C. J., Arsenault, K., Cosgrove, B., Radakovich, J.,
864 Bosilovich, M., Entin, J. K., Walker, J. P., Lohmann, D. and Toll, D.: The global land data assimilation system, *Bull. Amer.*
865 *Meteor. Soc.*, 85(3), 381–394, <https://doi.org/10.1175/BAMS-85-3-381>, 2004.

866 Serpelloni, E., Faccenna, C., Spada, G., Dong, D. and Williams, S. D. P.: Vertical GPS ground motion rates in the Euro-
867 Mediterranean region: New evidence of velocity gradients at different spatial scales along the Nubia-Eurasia plate boundary,
868 *J. Geophys. Res. Solid Earth*, 118(11), 6003–6024, <https://doi.org/10.1002/2013JB010102>, 2013.

869 Serpelloni, E., Vannucci, G., Anderlini, L. and Bennett, R. A.: Kinematics, seismotectonics and seismic potential of the eastern
870 sector of the European Alps from GPS and seismic deformation data, *Tectonophysics*, 688, 157–181,
871 <https://doi.org/10.1016/j.tecto.2016.09.026>, 2016.

872 Serpelloni, E., Pintori, F., Gualandi, A., Scoccimarro, E., Cavaliere, A., Anderlini, L., Belardinelli, M. E. and Todesco, M.:
873 Hydrologically Induced Karst Deformation: Insights From GPS Measurements in the Adria-Eurasia Plate Boundary Zone, *J.*
874 *Geophys. Res. Solid Earth*, 123(5), 4413–4430, <https://doi.org/10.1002/2017JB015252>, 2018.

875 Silverii, F., Pulvirenti, F., Montgomery-Brown, E. K., Borsa, A. A. and Neely, W. R.: The 2011-2019 Long Valley Caldera
876 inflation: New insights from separation of superimposed geodetic signals and 3D modeling, *Earth and Planetary Science*
877 *Letters*, 569, 117055, <https://doi.org/10.1016/j.epsl.2021.117055>, 2021.

878 Sternai, P., Sue, C., Husson, L., Serpelloni, E., Becker, T. W., Willett, S. D., Faccenna, C., Di Giulio, A., Spada, G., Jolivet,
879 L., Valla, P., Petit, C., Nocquet, J.-M., Walpersdorf, A. and Castellort, S.: Present-day uplift of the European Alps: Evaluating
880 mechanisms and models of their relative contributions, *Earth-Science Reviews*, 190, 589–604,
881 <https://doi.org/10.1016/j.earscirev.2019.01.005>, 2019.

882 Tan, W., Dong, D. and Chen, J.: Application of independent component analysis to GPS position time series in Yunnan

883 Province, southwest of China, *Advances in Space Research* 69(11), 4111-4122, <https://doi.org/10.1016/j.asr.2022.03.016>.

884 Tape, C., Musé, P., Simons, M., Dong, D. and Webb, F.: Multiscale estimation of GPS velocity fields. *Geophysical Journal*
885 *International* 179, 945–971. <https://doi.org/10.1111/j.1365-246X.2009.04337.x>, 2009.

886 Tiampo, K. F., Rundle, J. B., Klein, W., Ben-Zion, Y. and McGinnis, S.: Using eigenpattern analysis to constrain seasonal
887 signals in southern california, *Pure appl. geophys.*, 161(9–10), <https://doi.org/10.1007/s00024-004-2545-y>, 2004.

888 Tian, Y. and Shen, Z.: Extracting the regional common-mode component of GPS station position time series from dense
889 continuous network, *J. Geophys. Res. Solid Earth*, 121(2), 1080–1096, <https://doi.org/10.1002/2015JB012253>, 2016.

890 Tian, Y. and Shen, Z.: Correlation weighted stacking filtering of common-mode component in GPS observation network, *Acta*
891 *Seismologica Sinica*, 33(2), 198-208, 2011.

892 Vicente-Serrano, S. M. and López-Moreno, J. I.: Nonstationary influence of the North Atlantic Oscillation on European
893 precipitation, *J. Geophys. Res.*, 113(D20), <https://doi.org/10.1029/2008JD010382>, 2008.

894 Wdowinski, S., Bock, Y., Zhang, J., Fang, P. and Genrich, J.: Southern California permanent GPS geodetic array: Spatial
895 filtering of daily positions for estimating coseismic and postseismic displacements induced by the 1992 Landers earthquake,
896 *J. Geophys. Res.*, 102(B8), 18057–18070, <https://doi.org/10.1029/97JB01378>, 1997.

897 Yan, J., Dong, D., Bürgmann, R., Materna, K., Tan, W., Peng, Y. and Chen, J.: Separation of sources of seasonal uplift in
898 china using independent component analysis of GNSS time series, *J. Geophys. Res. Solid Earth*, 124(11), 11951–11971,
899 <https://doi.org/10.1029/2019JB018139>, 2019.

900 Yuan, P., Jiang, W., Wang, K. and Sneeuw, N.: Effects of spatiotemporal filtering on the periodic signals and noise in the GPS
901 position time series of the crustal movement observation network of china, *Remote Sens (Basel)*, 10(9), 1472,
902 <https://doi.org/10.3390/rs10091472>, 2018.

903 Zhang, K., Wang, Y., Gan, W. and Liang, S.: Impacts of local effects and surface loads on the common mode error filtering
904 in continuous GPS measurements in the northwest of yunnan province, china., *Sensors*, 20(18),
905 <https://doi.org/10.3390/s20185408>, 2020.

906 Zhu, Z., Zhou, X., Deng, L., Wang, K. and Zhou, B.: Quantitative analysis of geophysical sources of common mode component
907 in CMONOC GPS coordinate time series, *Adv. Space Res.*, 60(12), 2896–2909, <https://doi.org/10.1016/j.asr.2017.05.002>,
908 2017.